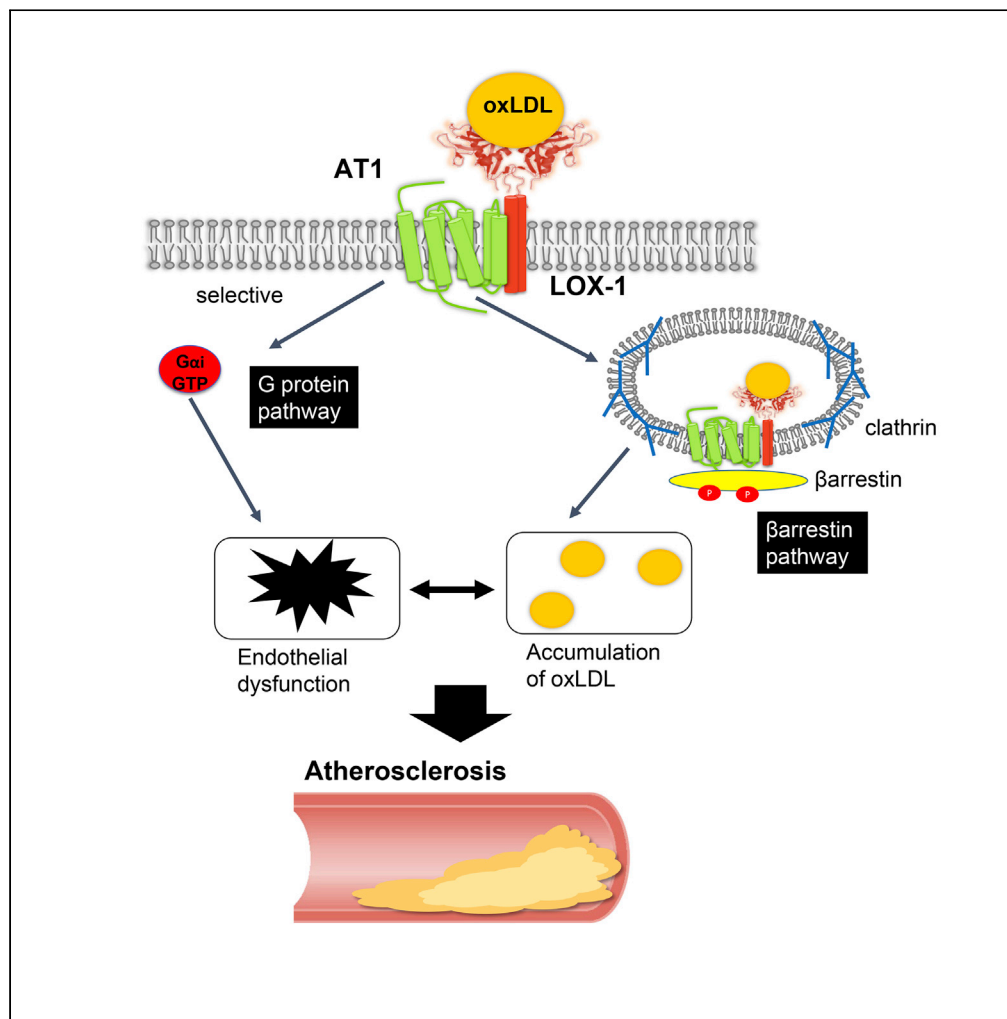**Article**

The endocytosis of oxidized LDL via the activation of the angiotensin II type 1 receptor

Toshimasa
Takahashi, Yibin
Huang, Koichi
Yamamoto, ...,
Herbert Y.
Gaisano, Tatsuya
Sawamura, Hiromi
Rakugi

kyamamoto@geriat.med.
osaka-u.ac.jp

HIGHLIGHTS
The binding of oxidized
LDL (oxLDL) to LOX-1
induces selective
activation of AT1

oxLDL and angiotensin II
additively or
competitively activate
AT1 in different cells

oxLDL promotes
β-arrestin-dependent
internalization of oxLDL-
LOX-1-AT1 complex

iScience

Article

The endocytosis of oxidized LDL via the activation of the angiotensin II type 1 receptor

Toshimasa Takahashi,[1,2,4] Yibin Huang,[1,4] Koichi Yamamoto,[1,5,*] Go Hamano,[1] Akemi Kakino,[3] Fei Kang,[2] Yuki Imaizumi,[1] Hikari Takeshita,[1] Yoichi Nozato,[1] Satoko Nozato,[1] Serina Yokoyama,[1] Motonori Nagasawa,[1] Tatsuo Kawai,[1] Masao Takeda,[1] Taku Fujimoto,[1] Kazuhiro Hongyo,[1] Futoshi Nakagami,[1] Hiroshi Akasaka,[1] Yoichi Takami,[1] Yasushi Takeya,[1] Ken Sugimoto,[1] Herbert Y. Gaisano,[2] Tatsuya Sawamura,[3] and Hiromi Rakugi[1]

SUMMARY

Arrestin-dependent activation of a G-protein-coupled receptor (GPCR) triggers endocytotic internalization of the receptor complex. We analyzed the interaction between the pattern recognition receptor (PRR) lectin-like oxidized low-density lipoprotein (oxLDL) receptor (LOX-1) and the GPCR angiotensin II type 1 receptor (AT1) to report a hitherto unidentified mechanism whereby internalization of the GPCR mediates cellular endocytosis of the PRR ligand. Using genetically modified Chinese hamster ovary cells, we found that oxLDL activates Gαi but not the Gαq pathway of AT1 in the presence of LOX-1. Endocytosis of the oxLDL-LOX-1 complex through the AT1-β-arrestin pathway was demonstrated by real-time imaging of the membrane dynamics of LOX-1 and visualization of endocytosis of oxLDL. Finally, this endocytotic pathway involving GPCR kinases (GRKs), β-arrestin, and clathrin is relevant in accumulating oxLDL in human vascular endothelial cells. Together, our findings indicate that oxLDL activates selective G proteins and β-arrestin-dependent internalization of AT1, whereby the oxLDL-LOX-1 complex undergoes endocytosis.

INTRODUCTION

Seven-transmembrane G-protein-coupled receptors (GPCRs) have long been attractive targets for drug discovery and development, as evidenced by the fact that about one-third of all drug targets are GPCRs (Santos et al., 2017). In addition to canonical activation by binding of the cognate ligand, recent understanding of the allosteric activation pathways of GPCRs has revealed the diversity in the physiological and pathological roles of this receptor family (Gentry et al., 2015; Khoury et al., 2014; Wootten et al., 2013). The allosteric activation of GPCRs is primarily induced by ligand binding to the allosteric ligand-binding domains of the GPCR (Gentry et al., 2015; Khoury et al., 2014; Wootten et al., 2013). The allosteric ligands of GPCRs trigger a cellular response distinct from that elicited by orthosteric ligands by differentially regulating activation of G proteins and arrestins, the latter primarily mediating cellular trafficking of receptor complexes (Jean-Charles et al., 2017; Ranjan et al., 2017; Smith and Rajagopal, 2016).

We recently reported that the angiotensin II type 1 receptor (AT1), a member of the class A GPCR family, forms a complex with the single transmembrane lectin-like oxidized low-density lipoprotein (oxLDL) receptor LOX-1 on the cellular membrane and thereby mediates oxLDL-induced AT1 activation, leading to vascular endothelial dysfunction in mice (Yamamoto et al., 2015). It has been increasingly recognized that heterodimerization of GPCRs could bias the signaling pathway of the partner receptor (Ferre et al., 2014; Forrester et al., 2018). It has also been reported that ligand binding to GPCRs triggers signal transduction modified by interactions with non-GPCRs, such as ion channels (Hermosilla et al., 2017; Shenoy and Lefkowitz, 2011; Shukla et al., 2010). However, our previous study is the only example of ligand binding to single transmembrane receptor-induced activation of an adjacent GPCR in the oligomeric complex (Yamamoto et al., 2015). Therefore, the precise molecular pathways that are activated upon stimulation remain largely undetermined in this case.

[1]Department of Geriatric and General Medicine, Osaka University Graduate School of Medicine, 2-2 Yamadaoka, Suita, Osaka, 565-0871, Japan

[2]Department of Medicine, University of Toronto, Toronto, Ontario M5S1A8, Canada

[3]Department of Molecular Pathophysiology, Shinshu University Graduate School of Medicine, Matsumoto, Nagano 390-8621, Japan

[4]These authors contributed equally

[5]Lead contact

*Correspondence: kyamamoto@geriat.med.osaka-u.ac.jp

The binding of AT1 to its original ligand angiotensin II (Ang II) triggers various cellular responses, primarily by activating specific G proteins, including Gαq/11, Gαi/0, and Gα12/13, with Gαq/11 being responsible for Ang II-induced arterial contraction (Berk, 1999; Hunyady and Catt, 2006). Since oxLDL is not a potent vaso-constrictor, it is conceivable that the G protein activation of AT1 by oxLDL is distinct from that by Ang II.

Internalization and intracellular trafficking of AT1 mediated by its interaction with β-arrestins (ARRBs) are the cellular responses of desensitization to prolonged Ang II stimulation (Hunyady, 1999; Hunyady et al., 2000). However, this also functions as a transport system for molecules adjacent to the receptor. Accumulation of oxLDL in atherosclerotic lesions is a major observation in the development of atherosclerosis (Steinberg, 1997; Steinberg and Witztum, 2010). Considering the pathophysiological importance of the intracellular accumulation of oxLDL in atherosclerosis, it is worth clarifying whether oxLDL binding to LOX-1 can trigger AT1 internalization, translocation of the oxLDL-LOX-1-AT1 complex, and eventually lead to intracellular accumulation of oxLDL.

In the present study, we investigated two topics: (1) whether oxLDL induces the activation of the same G protein as Ang II and (2) whether oxLDL-induced AT1 activation causes the cellular accumulation of oxLDL.

RESULTS

oxLDL-induced activation of AT1 is G protein selective

In this study, we used five different genetically engineered Chinese hamster ovary (CHO) cells that endoge-nously express neither LOX-1 nor AT1 to individually analyze the G protein and β-arrestin pathways of oxLDL-induced AT1 activation. CHO cells expressing either human (h)AT1R or hLOX1 (CHO-AT1 and CHO-LOX-1, respectively), CHO cells expressing both hLOX-1 and hAT1 (CHO-LOX-1-AT1), CHO cells expressing both hLOX-1 and mutated hAT1 with impaired ability to activate G protein (Haendeler et al., 2000) (CHO-LOX-1-AT1 mutant with β-arrestin-biased signaling [CHO-LOX-1-AT1mβ]), and CHO cells expressing both hLOX-1 and mutated hAT1 with impaired ability to activate β-arrestin (CHO-LOX-1-AT1 mutant with G-pro-tein-biased signaling [CHO-LOX-1-AT1mg]) (Qian et al., 2001) (Figures 1A and 1B) were used. There was no dif-ference in the magnitude of membrane expression of these receptors among the respective cells, as assessed by cell-based enzyme-linked immunosorbent assay (ELISA) in non-permeabilized conditions (Figure 1C).

We previously found that the proximity between LOX-1 and AT1 on the cellular membrane was absent be-tween LOX-1 and the Ang II type receptor (AT2), which is the isoform of AT1, in an *in situ* proximity ligation assay (PLA), indicating that LOX-1 specifically binds to AT1 (Yamamoto et al., 2015). Similar red fluores-cence intensity was observed in *in situ* PLA in non-permeabilized conditions in CHO-LOX-1-AT1, CHO-LOX-1-AT1mβ, and CHO-LOX-1-AT1mg, suggesting that these AT1 mutants interact with LOX-1, similar to the interaction with intact AT1 on the cellular surface (Figure 1D).

These cells were used to investigate whether oxLDL could activate Gαi and Gαq, which interact with AT1, by quantifying the reduction in Forskolin-induced cyclic adenosine monophosphate (cAMP) accumulation and increase in inositol monophosphate (IP1) production, respectively. As shown in Figure 2A, oxLDL and Ang II decreased cAMP in CHO-LOX-1-AT1 in a dose-dependent manner, with an EC_{50} of 7.4 μg/mL and 10^{-8} M, respectively. A reduction in cAMP by 40 μg/mL oxLDL was not observed in either CHO-LOX1 or CHO-LOX-1-AT1 cells treated with the Gαi inhibitor pertussis toxin (PTX) (Figure 2B). G protein dependence of this phenomenon was also confirmed by the reduction in cAMP by oxLDL in CHO-LOX-1-AT1mg but not in CHO-LOX-1-AT1mβ (Figure 2B).

In contrast to the findings regarding Gαi signaling, oxLDL did not induce the activation of Gαq signaling through the LOX-1-AT1-dependent pathway, as shown by the lack of IP1 accumulation in response to high concentrations of oxLDL in CHO-LOX-1-AT1 (Figure 2D). As expected, Ang II dose dependently increased IP1 production in CHO-LOX-1-AT1, and the effect was highly reduced in CHO-LOX-1-AT1mβ but not in CHO-LOX-1-AT1mg (Figures 2C and 2D). These findings suggest that oxLDL-induced activation of AT1 is distinct from the Ang II-induced activation of AT1 in terms of G protein selectivity.

oxLDL induces cellular inflammation additively with Ang II via the AT1-G-protein-dependent pathway

We assessed cellular inflammation by detecting the activation of NF-κB using the dual luciferase reporter assay system in the genetically engineered CHO cells. As shown in Figure 3A, oxLDL dose dependently
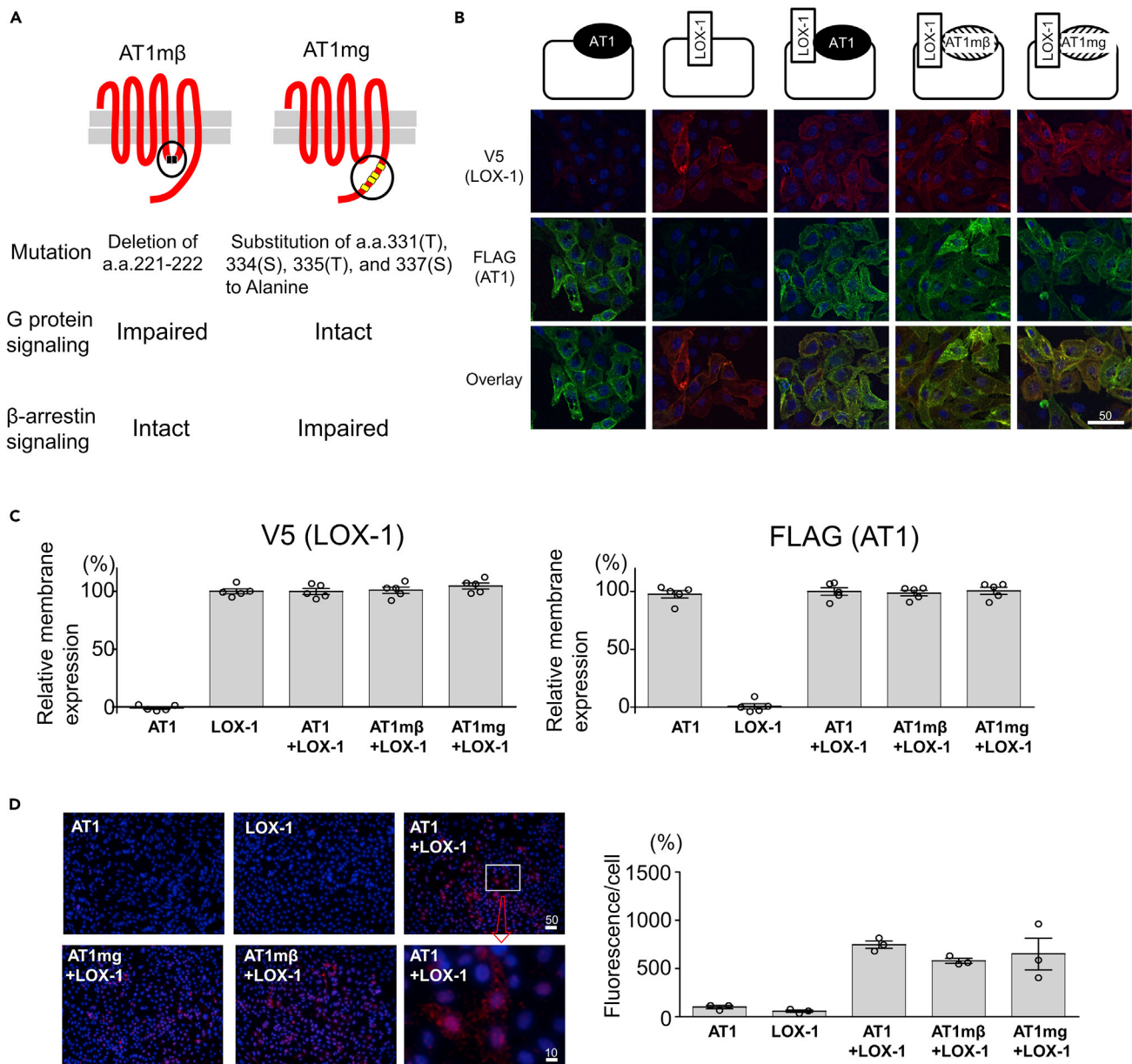
Figure 1. Generation of genetically engineered CHO cells expressing LOX-1 and/or AT1 or biased AT1 mutants

(A) Overview of two biased AT1 mutants.

AT1mβ, AT1 mutant with β-arrestin-biased signaling; AT1mg, AT1 mutant with G-protein-biased signaling.

(B) Immunofluorescence of CHO cells stably expressing V5-tagged LOX-1 and/or FLAG-tagged AT1 or biased AT1 mutants using anti-V5 or anti-FLAG antibodies. Scale bar (μm).

(C) Quantification of membrane-expressing V5-tagged LOX-1 and FLAG-tagged AT1 or biased AT1 mutants by cell-based ELISA. Absorbance in CHO cells expressing V5-tagged LOX-1 and FLAG-tagged AT1 (CHO-LOX-1-AT1) was normalized to 100% (n = 5, each). Data are represented as mean ± SEM. The differences were determined by one-way analysis of variance (ANOVA) with Bonferroni correction. *p < 0.01 vs. the other types of cells.

(D) *In situ* proximity ligation assay (PLA) of CHO cells stably expressing V5-tagged LOX-1 and/or FLAG-tagged AT1 or biased AT1 mutants using anti-V5 and anti-FLAG antibodies. Scale bar (μm).

The graph indicates the fluorescence/number of nuclei (% of that in CHO-AT1) (n = 3, each) Data are represented as mean ± SEM. The differences were determined by one-way ANOVA with Bonferroni correction. *p < 0.01 vs.CHO-AT1, CHO-LOX-1, †p < 0.05 vs.CHO-AT1, p < 0.01 vs. CHO-LOX-1.

increased the activation of NfκB in CHO-LOX-1-AT1 and CHO-LOX-1-AT1mg, and the activation was significantly attenuated in CHO-LOX-1-AT1mβ, suggesting that oxLDL-induced inflammatory response involves G-protein-dependent but not β-arrestin-dependent signaling pathway of AT1. We also found that
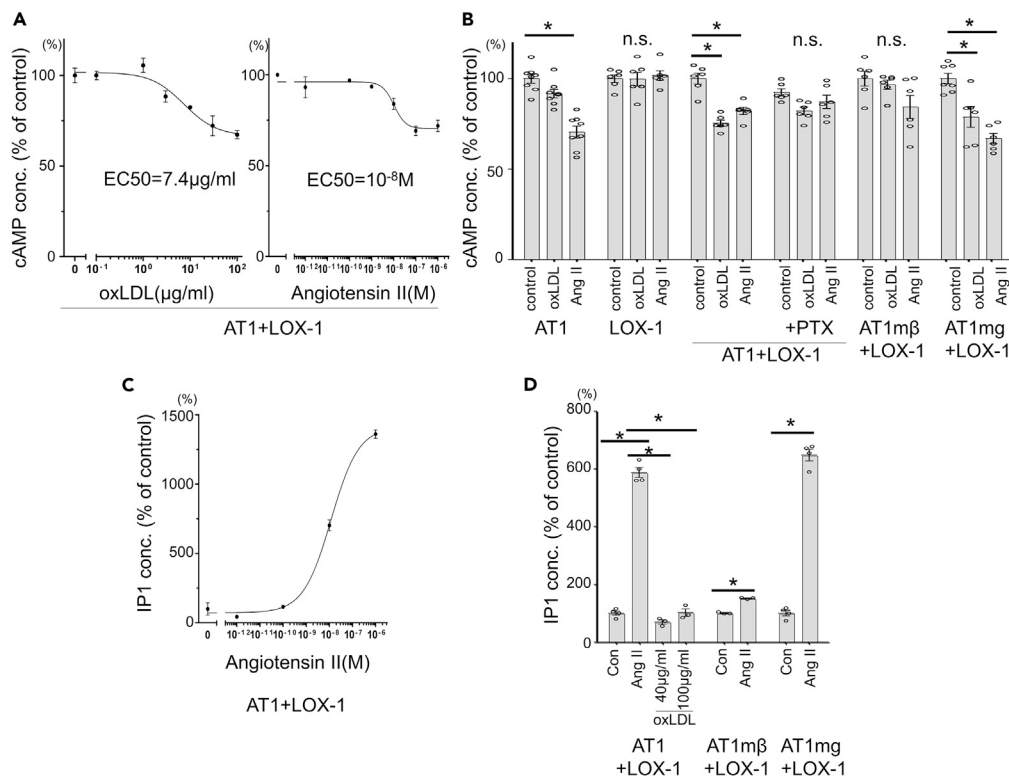
Figure 2. Assessment of Gαi and Gq signaling in genetically engineered CHO cells by quantifying reduction in Forskolin-induced cAMP accumulation and increase in IP1 production, respectively

(A) Dose-dependent response in cyclic adenosine monophosphate (cAMP) concentration in response to oxLDL or angiotensin II in CHO-LOX-1-AT1. Cells were treated with 1 μM forskolin to induce cAMP accumulation (n = 4, each). Data are represented as mean ± SEM.

(B) cAMP concentration in response to vehicle, 40 μg/mL oxLDL or 10^{-8} M angiotensin II in genetically engineered CHO cells. Gi inhibitor pertussis toxin (PTX) was pretreated at 25 ng/mL for 12 h before stimulation. The concentration in control-treated wells in each cell type was normalized to 100% (n = 6–8). Data are represented as mean ± SEM. The differences were determined by one-way analysis of variance (ANOVA) with Bonferroni correction. *p < 0.01.

(C) Dose-dependent response in inositol monophosphate (IP1) concentration in response to angiotensin II in CHO-LOX-1-AT1, expressed as percentage of IP1 concentration in the absence of angiotensin II (n = 4, each). Data are represented as mean ± SEM.

(D) IP1 concentration in response to vehicle, angiotensin II (10^{-7}M), or oxLDL in genetically engineered CHO cells. The concentration in control wells of each cell type was normalized to 100% (n = 4, each).

Data are represented as mean ± SEM. The differences were determined by one-way ANOVA with Bonferroni correction. *p < 0.01.

the activation of NfκB increased prominently in response to the combined treatment of Ang II with oxLDL compared to either treatment alone in CHO-LOX-1-AT1, suggesting that the Ang II-AT1 signaling and the oxLDL-LOX-1-AT1 signaling have additive effect on cellular inflammation in this cell condition (Figure 3B).

oxLDL induces internalization of LOX-1 and AT1 via a β-arrestin-dependent signaling pathway of AT1

To investigate whether the activation of AT1 by oxLDL induced internalization of the LOX-1-AT1 complex, we utilized a live cell imaging technique using a real-time spinning disk confocal super-resolution microscope in CHO-K1 cells transiently transfected with LOX-1 labeled with mScarlet and AT1 labeled with eGFP. As shown in the Video S1, we observed yellow puncta, indicating co-localization of AT1 and LOX-1 moving on the cell surface-focused image, with some of them disappearing after application of 10 μg/mL oxLDL, implying that the complex of LOX-1 and AT1 had been internalized. To quantify the internalization of LOX-1 in response to oxLDL stimulation, we analyzed the percentage of red LOX-1 puncta that vanished during treatment with vehicle or 10 μg/mL oxLDL, by comparing images before and 3 min after
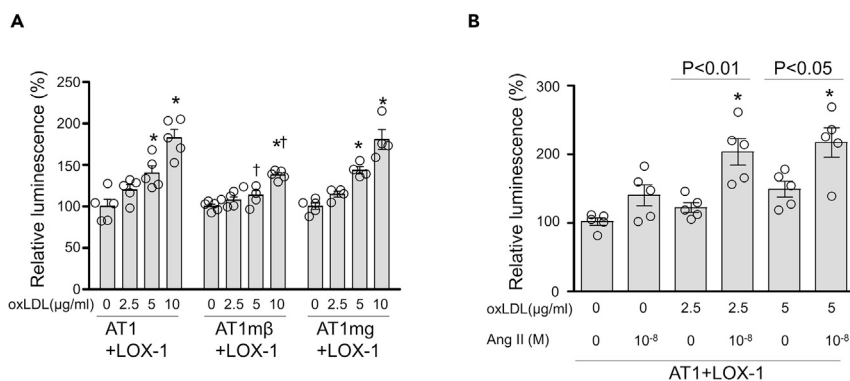
A

B

Figure 3. Assessment of NfkB activity in genetically engineered CHO cells

(A) NfκB activity detected by a luciferase reporter assay in CHO-LOX-1-AT1, CHO-LOX-1-AT1mβ, and CHO-LOX-1-AT1mg treated with different concentration of oxLDL for 24 hr. The relative luminescence (NfkB-luciferase/control-renilla) in each cell type treated with 0μg/ml oxLDL in each cell type was normalized to 100% (n = 5). Data are represented as mean ± SEM. The differences were determined by one-way analysis of variance (ANOVA) with Bonferroni correction. *p < 0.05 vs. 0μg/ml oxLDL.

†p < 0.05 vs. concentration-matched oxLDL in CHO-LOX-1-AT1mβ.

(B) NfκB activity detected by a luciferase reporter assay in CHO-LOX-1-AT1 treated with vehicle, 2.5, 5μg/ml oxLDL, 10^{-8} M Ang II, or oxLDL in combination with Ang II for 24 hr. The relative luminescence (NfkB-luciferase/control-renilla) in each cell type treated with 0μg/ml oxLDL in each cell type was normalized to 100% (n = 5). Data are represented as mean ± SEM. The differences were determined by one-way ANOVA with Bonferroni correction. *p < 0.01 vs. vehicle treatment.

application of each reagent in CHO cells expressing fluorescent-labeled receptors (Figures 4A and 4B). We found that oxLDL increased the number of vanished puncta in cells transfected with LOX-1 and AT1 but not in cells transfected with LOX-1 alone (Figure 4C). This phenomenon appeared to be β-arrestin dependent, as the increase in vanished LOX-1 puncta was similarly observed in response to oxLDL in cells transfected with LOX-1 and AT1mβ, but was totally dampened in cells transfected with LOX-1 and AT1mg (Figure 4C).

Intracellular accumulation of oxLDL depends on the concurrent presence of LOX-1 and AT1

We used fluorescent oxLDL (Dil-oxLDL) to monitor cellular accumulation of oxLDL as a consequence of LOX-1 internalization. The binding of oxLDL to the cellular membrane was monitored after 30 min incubation with Dil-oxLDL at 4°C (Figure 5A). As shown in Figure 5B, oxLDL binds to LOX-1 at the cellular membrane in a similar manner between CHO-LOX-1 and CHO-LOX-1-AT1. Endocytic traffic of oxLDL was detected in CHO-LOX-1-AT1, where co-localization of oxLDL with early and late endosomes and lysosomes was observed, and the co-localization with lysosomes increased over time following 30 min of Dil-oxLDL treatment (Figure S1). Cellular accumulation of oxLDL was monitored in CHO cells after application of Dil-oxLDL for 30 min followed by washing of membrane-bound oxLDL for 24 h at 37°C (Figure 5A). Cellular accumulation of Dil-oxLDL was competitively blocked by co-treatment with non-fluorescent oxLDL, suggesting that the accumulation is not induced by the non-specific accumulation of Dil fluorescent dye (Figure S2). We found that cellular (fluorescent) oxLDL content was consistently higher in CHO-LOX-1-AT1 than in CHO-AT1 and CHO-LOX-1 after application of 0.4, 2, and 10 μg/mL oxLDL (Figure 5C). While cellular oxLDL content was similar between CHO-AT1 and CHO-LOX-1 after the application of 2 μg/mL oxLDL, 10 μg/mL oxLDL accumulated more vigorously in CHO-LOX-1 than in CHO-AT1, suggesting the presence of AT1-independent uptake of oxLDL via LOX-1 (Figure 5C). Pretreatment with the LOX-1 antibody dampened the increased uptake of oxLDL in the LOX-1-expressing CHO cells (Figure 5C).

Intracellular accumulation of oxLDL in the presence of LOX-1 is stimulated by the activation of a β-arrestin-dependent signaling pathway of AT1

We found that oxLDL binding to LOX-1 on the cellular membrane was similarly observed in CHO-LOX-1-AT1, CHO-LOX-1-AT1mβ, and CHO-LOX-1-AT1mg cells (Figure 5D). As shown in Figure 5E, the cellular oxLDL content after the application of 2 μg/mL Dil-oxLDL was higher in CHO-LOX-1-AT1 and CHO-LOX-1-AT1mβ than in CHO-LOX-1-AT1mg and CHO-LOX-1, suggesting that the uptake of oxLDL through AT1 was β-arrestin dependent (Figure 5E). The mechanism was further confirmed using transfection of dominant negative (DN) β-arrestin (Krupnick et al., 1997) as compared to that of the negative control vector harboring mutated DN-β-arrestin, in
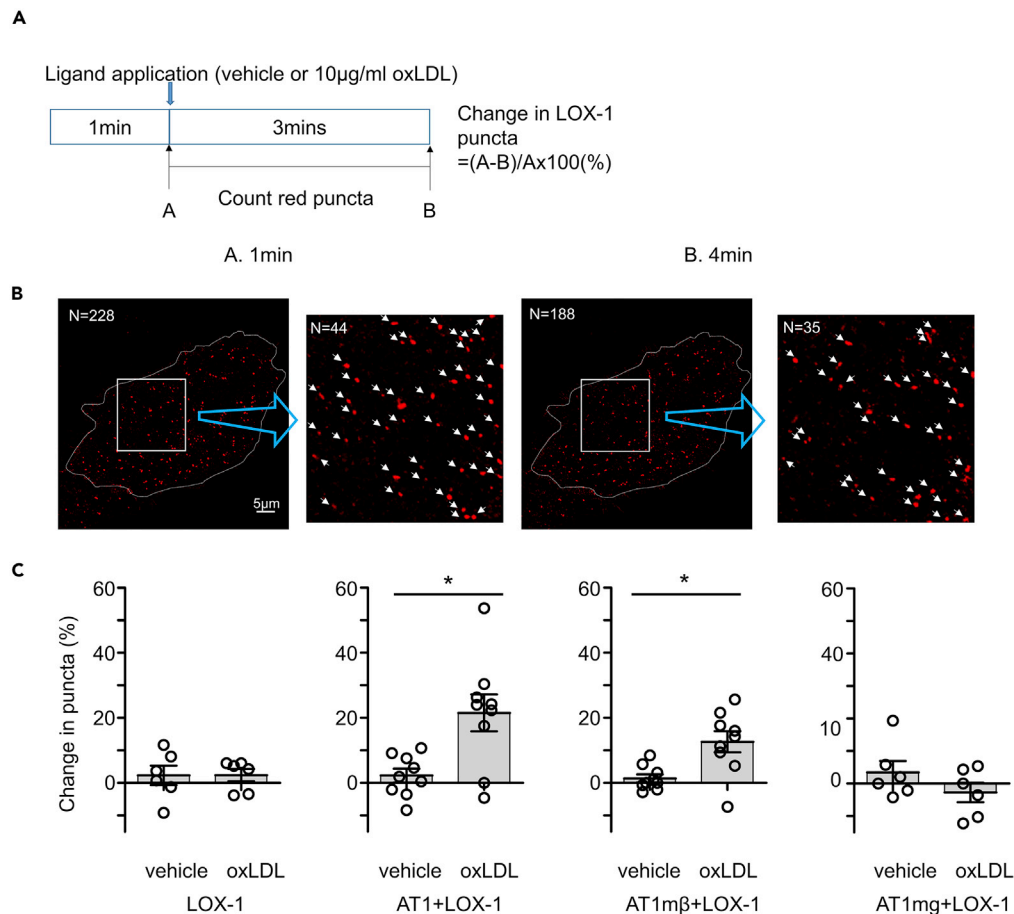
Figure 4. AT1-β-arrestin-dependent internalization of membrane LOX-1 in response to oxLDL treatment

(A) Calculation of change in red puncta of LOX-1. Real-time membrane imaging of CHO-K1 cells co-transfected with LOX-1-mScarlet and control, AT1, AT1mβ, or AT1mg labeled with eGFP (Video S1). A count of puncta was performed using separated images visualizing LOX-1-scarlet just before and 3 min after ligand application.

(B) Example of counting red puncta in CHO-K1 cells co-expressing LOX-1-scarlet and AT1-GFP applied with oxLDL. In this case, the change in LOX-1 puncta is $(228 - 188)/288 \times 100 = 17.5\%$.

(C) Change in LOX-1 puncta in CHO-K1 cells expressing the indicated receptors (n = 6–9).

Data are represented as mean $\pm$ SEM. The difference between the application of vehicle and oxLDL was determined by Student's t-test. *p < 0.01.

which the clathrin-binding domain was deleted (Kang et al., 2009), or barbadin, an inhibitor of the β-arrestin/AP2 endocytic complex (Beautrait et al., 2017) (Figures 5F and 5G). Transfection of DN β-arrestin decreased the uptake of 2 μg/mL oxLDL in CHO-LOX-1-AT1 compared to that in cells transfected with the negative control vector, while no difference was observed in similarly treated CHO-LOX-1, further supporting the β-arrestin-dependent uptake of oxLDL through AT1 (Figure 5F). A similar effect of DN-β-arrestin was observed upon treatment with 10 μg/mL oxLDL in CHO-LOX-1-AT1 but not CHO-LOX-1, suggesting that the AT1-independent uptake of a higher concentration of oxLDL via LOX-1 (Figure 5C) was β-arrestin independent (Figure S3). The β-arrestin-induced endocytosis of oxLDL was also supported by barbadin, which inhibits the accumulation of oxLDL in CHO-LOX-1-AT1 but not in CHO-LOX-1 (Figure 5G). We confirmed that the cellular accumulation of oxLDL does not depend on Gαi or Gαq-dependent pathways, as pharmacological inhibitors of Gαq and Gαi had no effect on oxLDL accumulation in CHO-LOX-1-AT1 (Figure S4).

LOX-1-AT1-β-arrestin-dependent oxLDL uptake is relevant in human vascular endothelial cells

We explored the biological relevance of the LOX-1-AT1-β-arrestin-dependent uptake of oxLDL in human vascular endothelial cells (Figure 6A). Similar to the findings in CHO-LOX-1-AT1 (Figure S1), endocytic traffic
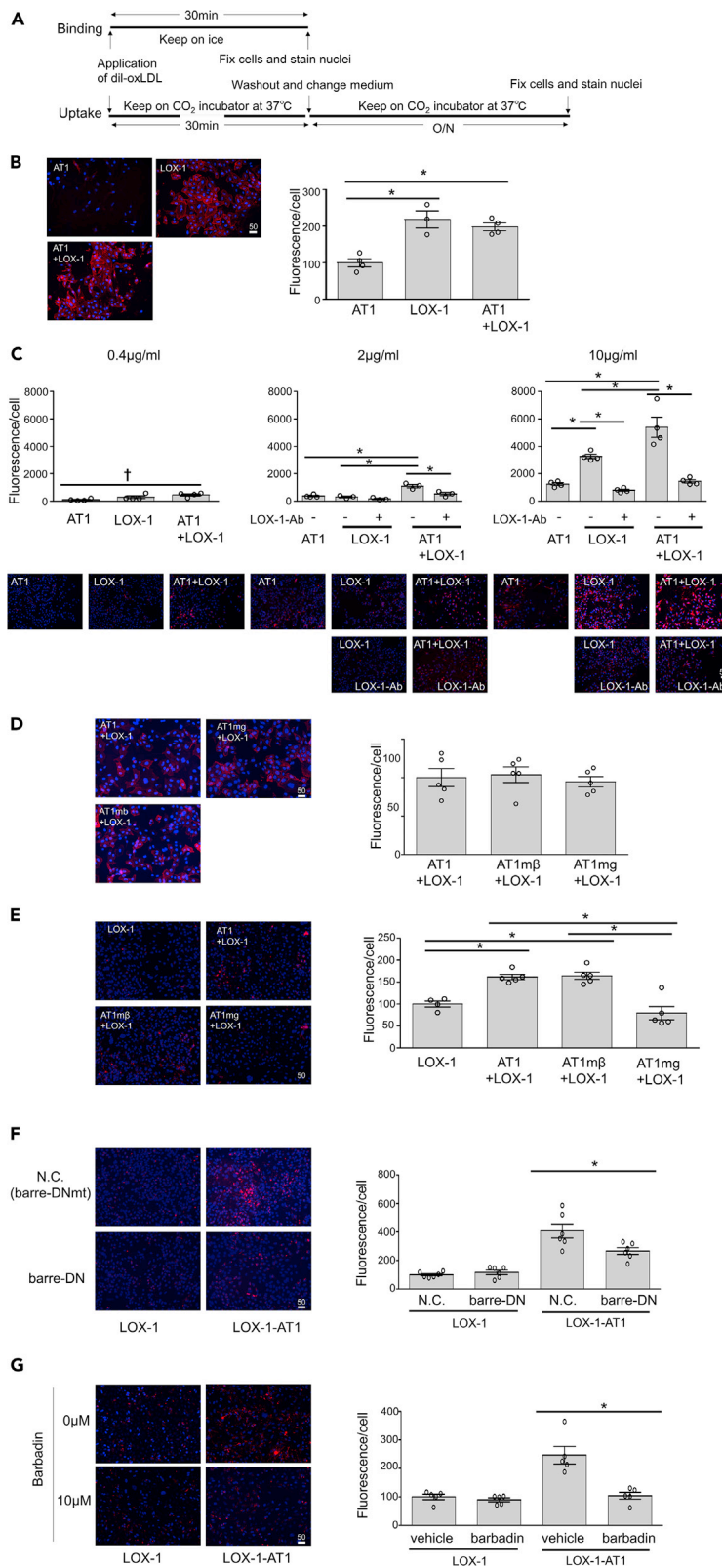
Figure 5. LOX-1-AT1-β-arrestin-dependent uptake of oxLDL in genetically engineered CHO cells

(A) Protocol of visualization of membrane binding and intracellular uptake of Dil-labeled oxLDL in genetically engineered CHO cells.

(B) Binding of 2 μg/mL Dil-labeled oxLDL in the indicated genetically engineered CHO cells (n = 4, each). Scale bar, μm. The graph indicates the fluorescence/number of nuclei, and the average value of the group at the far left was normalized to 100%. Data are represented as mean ± SEM. The differences were determined by one-way analysis of variance (ANOVA) with Bonferroni correction. *p < 0.01.

(C) Intracellular uptake of the indicated concentration of Dil-labeled oxLDL in the indicated genetically engineered CHO cells. LOX-1 neutralizing antibody, TS92, was used to pretreat the cells at 10 μg/mL for 30 min before stimulation (n = 4, each). Scale bar, μm. The graph indicates the fluorescence/number of nuclei, and the average value of the group at the far left was normalized to 100%. Data are represented as mean ± SEM. The differences were determined by one-way ANOVA with Bonferroni correction. *p < 0.01, †p < 0.05.

(D) Binding of 2 μg/mL Dil-labeled oxLDL in the indicated genetically engineered CHO cells (n = 5, each). Scale bar, μm. The graph indicates the fluorescence/number of nuclei, and the average value of the group at the far left was normalized to 100%. Data are represented as mean ± SEM. The differences were determined by one-way ANOVA.

(E) Intracellular uptake of 2 μg/mL Dil-labeled oxLDL in the indicated genetically engineered CHO cells (n = 5, each). Scale bar, μm. The graph indicates the fluorescence/number of nuclei, and the average value of the group at the far left was normalized to 100%. Data are represented as mean ± SEM. The differences were determined by one-way ANOVA with Bonferroni correction. *p < 0.01.

(F) Intracellular uptake of 2 μg/mL Dil-labeled oxLDL in the indicated genetically engineered CHO cells transfected with dominant negative vector of β-arrestin (barre-DN) or negative control vector (N.C.) (n = 5, each). The vectors were transfected 24 h before stimulation with Dil-labeled oxLDL.

Schematics of barre-DN and N.C. are shown in Figure 3 (E). Scale bar, μm.

The graph indicates the fluorescence/number of nuclei, and the average value of the group at the far left was normalized to 100%. Data are represented as mean ± SEM. The differences were determined by one-way ANOVA with Bonferroni correction. *p < 0.01.

(G) Intracellular uptake of 2 μg/mL Dil-labeled oxLDL in the indicated genetically engineered CHO cells pretreated with vehicle or the β-arrestin-specific inhibitor barbadin at 10 μM for 30 min (n = 5, each). Scale bar, μm. The graph indicates the fluorescence/number of nuclei, and the average value of the group at the far left was normalized to 100%.

Data are represented as mean ± SEM. The differences were determined by one-way ANOVA with Bonferroni correction. *p < 0.01.

of oxLDL was detected in human umbilical vein endothelial cells (HUVECs). In these cells, co-localization of oxLDL with early and late endosomes and lysosomes was observed, which increased over time after 30 min of Dil-oxLDL treatment for late endosomes and lysosomes (Figure S5). We found that oxLDL accumulated in HUVECs and human aortic endothelial cells (HAECs) after the application of 2 μg/mL Dil-oxLDL for 6 h followed by washing for 24 h (Figure 6B). Genetic knockdown of AT1 or LOX-1 by small interfering RNA (siRNA) prior to Dil-oxLDL application similarly inhibited the accumulation of oxLDL in these cells (Figure 6B, knockdown efficiency shown in Figure S6A). Simultaneous knockdown of AT1 and LOX-1 had no additional effect compared to the knockdown of each gene alone, suggesting that both receptors share the same pathway for oxLDL uptake (Figure 6B). The inhibitory effect of siRNA against AT1 or LOX-1 was also observed in these cells, even after a quick Dil-oxLDL treatment (10 min or 30 min), suggesting the rapid kinetics of this phenomenon (Figure S7). It was recently reported that SR-B1 promotes transcytosis of both native LDL and oxLDL in endothelial cells (Huang et al., 2019). Consistently, we found that siRNA targeting SCARB1, the gene encoding SR-BI, inhibited the accumulation of Dil-oxLDL to a similar to siRNA targeting AT1 or LOX-1 (Figure 6C, knockdown efficiency shown in Figure S6B). In contrast, pre- and co-treatment with 20 μg/mL native LDL hampered this inhibitory effect of siRNA on SCARB1, whereas such treatments did not influence the effect of siRNA on AT1 or LOX-1 (Figure 6C). This result is consistent with the binding specificity of LOX-1 for modified LDL. We also found that knockdown of β-arrestin 1 (ARRB1) and/or β-arrestin 2 (ARRB2) inhibited the accumulation of oxLDL in HUVECs and HAECs to a similar extent as observed in cells with knockdown of AT1 (Figure 6D). β-arrestin-dependent uptake of oxLDL in endothelial cells was further supported by DN or pharmacological inhibition of β-arrestin, both of which inhibited the uptake of oxLDL in HUVECs and HAECs (Figures 6E and 6F). β-arrestin is known to mediate G-protein-independent activation of extracellular signal-regulated kinase 1/2 by Ang II (Lee et al., 2008). In line with the literature, we found that the activation of ERK1/2 in HUVECs, triggered by a 10-min treatment with oxLDL, was inhibited, at least partially, by treatment with barbadin, while this phenomenon did not occur in presence of the Gαi inhibitor PTX, consistent with our previous study (Yamamoto et al., 2015) (Figure S8). We also found that the activation of ERK 1/2 by the co-treatment of 20μg/ml oxLDL with 10^{-7} MAng II was equivalent to that by Ang II alone and lower than that by oxLDL alone in HUVECs, suggesting that the effect of Ang II and oxLDL on cellular signaling is not additive but rather competitive in certain experimental condition in endothelial cells (Figure S9).
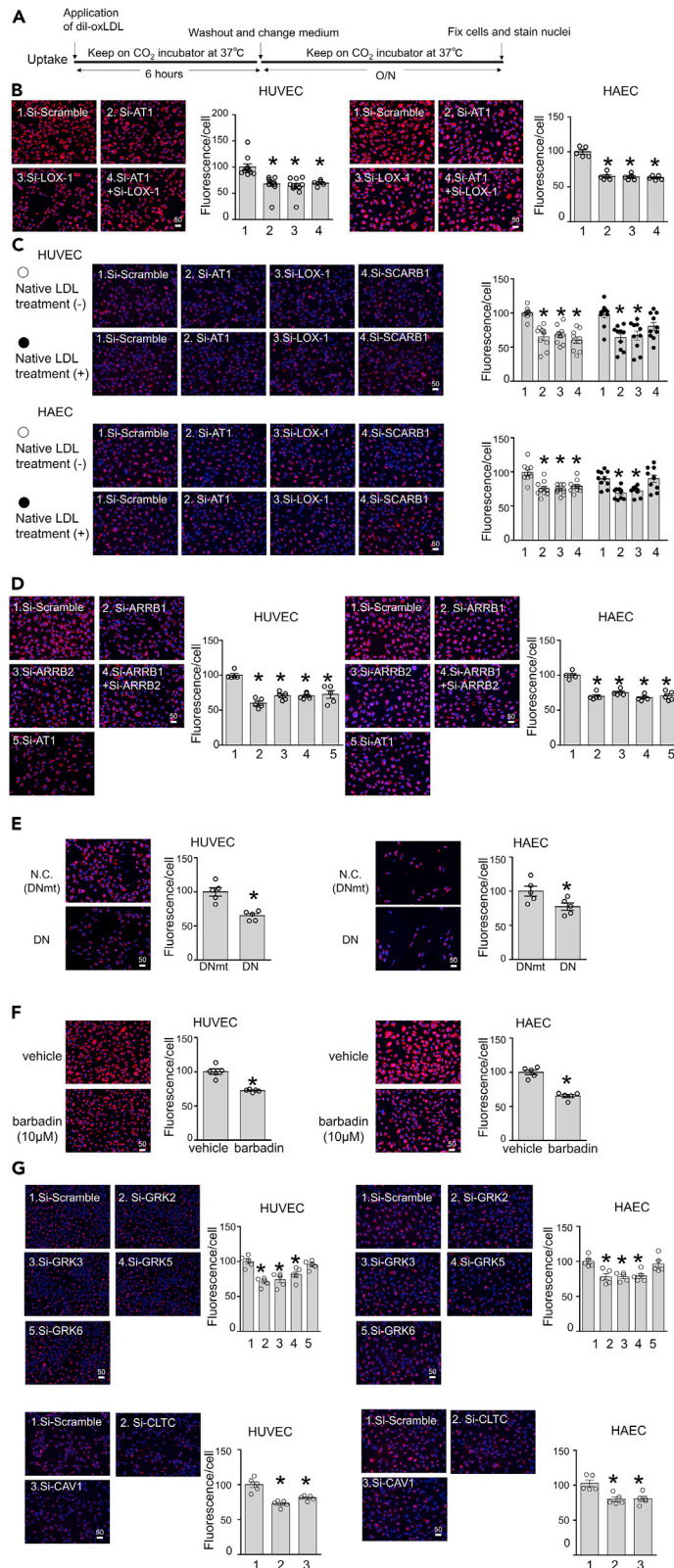
Figure 6. LOX-1-AT1-β-arrestin-dependent uptake of oxLDL in human endothelial cells

(A) Protocol for visualization of intracellular uptake of Dil-labeled oxLDL in human umbilical vein endothelial cells (HUVECs) and human aortic endothelial cells (HAECs).

(B) Intracellular uptake of 2 μg/mL Dil-labeled oxLDL in cells with siRNA knockdown of indicated genes (n = 5, each). Scale bar, μm. The graph indicates the fluorescence/number of nuclei, and the average value of the group at the far left was normalized to 100%. Data are represented as mean ± SEM. The differences were determined by one-way analysis of variance (ANOVA) with Bonferroni correction. *p < 0.01 vs. control. The knockdown efficiency of each gene was demonstrated in Figure S6.

(C) Intracellular uptake of 2 μg/mL Dil-labeled oxLDL in cells with siRNA-mediated knockdown of the indicated genes, pre- and co-treated or not with non-labeled native LDL at 20 μg/mL (n = 10, each). Pretreatment with native LDL was carried out for 1 hr. Scale bar, μm. The graph indicates the fluorescence/number of nuclei, and the average value of the group at the far left was normalized to 100%. Data are represented as mean ± SEM. The differences were determined by one-way ANOVA with Bonferroni correction. *p < 0.01 vs. control. The knockdown efficiency of each gene was demonstrated in Figure S6.

(D) Intracellular uptake of 2 μg/mL Dil-labeled oxLDL in cells with siRNA-mediated knockdown of the indicated genes (n = 5, each). Scale bar, μm. The graph indicates the fluorescence/number of nuclei, and the average value of the group at the far left was normalized to 100%.

Data are represented as mean ± SEM. The differences were determined by one-way ANOVA with Bonferroni correction. *p < 0.01 vs. control. The knockdown efficiency of each gene was demonstrated in Figure S6.

(E) Intracellular uptake of 2 μg/mL Dil-labeled oxLDL in cells transfected with dominant negative vector of β-arrestin (barre-DN) or negative control vector (N.C.) (n = 5, each). Scale bar, μm. The graph indicates the fluorescence/number of nuclei, and the average value of the group at the far left was normalized to 100%.

Data are represented as mean ± SEM. The differences were determined by Student's t-test. *p < 0.01 vs. control (DNmt).

(F) Intracellular uptake of 2 μg/mL Dil-labeled oxLDL in cells pretreated with vehicle or the β-arrestin-specific inhibitor barbadin at 10 μM for 30 min (n = 5, each).

The graph indicates the fluorescence/number of nuclei, and the average value of the group at the far left was normalized to 100%. Scale bar, μm.

The graph indicates the fluorescence/number of nuclei, and the average value of the group at the far left was normalized to 100%.

Data are represented as mean ± SEM. The differences were determined by Student's t-test. *p < 0.01 vs. control.

(G and H) Intracellular uptake of 2 μg/mL Dil-labeled oxLDL in cells with siRNA-mediated knockdown of the indicated genes (n = 5, each). Scale bar, μm.

The graph indicates the fluorescence/number of nuclei, and the average value of the group at the far left was normalized to 100%. Data are represented as mean ± SEM. The differences were determined by one-way ANOVA with Bonferroni correction. *p < 0.01 vs. control. The knockdown efficiency of each gene was demonstrated in Figure S6.

GPCR kinases and clathrin are involved in oxLDL uptake by human vascular endothelial cells

The interaction of GPCR kinases (GRKs) with the cytoplasmic tail of AT1 is a crucial step for Ang II-induced AT1 internalization, followed by β-arrestin recruitment (Grisanti et al., 2018; Sato et al., 2015). Therefore, we used siRNA-mediated knockdown of genes encoding the four major isoforms of GRKs (GRK2, GRK3, GRK5, and GRK6) to investigate the involvement of these proteins in the uptake of oxLDL by endothelial cells (Kim et al., 2005; Oppermann et al., 1996). We found that siRNA targeting *GRK2* or *GRK3* decreased gene expression each other (Figure S6C). siRNA targeting *GRK2*, *GRK3*, or *GRK5* inhibited oxLDL uptake in HUVECs and HAECs, whereas siRNA targeting *GRK6* had no effect on this process (Figure 6G, knockdown efficiency shown in Figure S6C). Although Ang II-induced AT1 internalization occurs via clathrin-dependent endocytosis, Murphy et al. reported the presence of LOX-1- and clathrin-independent mechanisms of oxLDL uptake (Murphy et al., 2008). Therefore, as caveolae-mediated endocytosis of oxLDL was observed in HUVECs (Sun et al., 2010), we tested whether the uptake of oxLDL in endothelial cells was affected by siRNA-mediated knockdown of *CHC17* or caveolin-1, encoding the key molecules for the formation of clathrin or caveolae, respectively. We found that siRNA targeting either *CHC17* or caveolin-1 inhibited the uptake of Dil-oxLDL in HUVECs and HAECs, suggesting the involvement of both clathrin-dependent and clathrin-independent pathways in the endocytosis of oxLDL (Figure 6H, knockdown efficiency shown in Figure S6D).

Pharmacological blockade of AT1 has no effect on β-arrestin-dependent internalization of the oxLDL-LOX-1-AT1 complex

We previously reported that G-protein-dependent cell signaling of AT1 provoked by the binding of oxLDL to LOX-1 is inhibited by treatment with AT1 blockers (ARBs) that competitively bind to the Ang II-binding pocket of AT1 (Yamamoto et al., 2015). Finally, we tested whether ARBs could inhibit the β-arrestin-dependent internalization of the oxLDL-LOX-1-AT1 complex. As a result, pretreatment with a high concentration

(10 μM) of ARBs, losartan, telmisartan, or irbesartan had no effect on oxLDL uptake in CHO-LOX-1-AT1 or HUVECs (Figure S10).

DISCUSSION

In the current study, we found that the activation of AT1 by the binding of oxLDL to LOX-1 is distinct from the activation of AT1 by its orthosteric ligand Ang II, in terms of its selectivity in G protein signaling and the biological significance of β-arrestin-dependent receptor internalization. Given that Ang II elicits its pressor action primarily by Gq-dependent activation of AT1, the absence of AT1-Gq activation by oxLDL can answer the question raised in our previous study (Yamamoto et al., 2015) regarding the lack of association between hypertension and elevated circulating oxLDL concentration in patients with atherosclerosis (Toshima et al., 2000).

Clathrin-mediated endocytosis of AT1 via a β-arrestin-dependent pathway is widely recognized as a cellular desensitization process by which the response to repetitive stimulation of Ang II is attenuated (Turu et al., 2006; Violin and Lefkowitz, 2007). Our current findings strongly suggest that oxLDL triggers the activation of GRKs, followed by β-arrestin-induced clathrin-dependent endocytosis of the AT1-LOX-1 complex, whereby circulating oxLDL is translocated into vascular endothelial cells. The uptake of oxLDL in the vascular endothelium by LOX-1 is involved in the development of atherosclerosis (Kita et al., 2001; Li and Mehta, 2005; Mehta et al., 2006). Our findings raise the possibility that AT1-mediated internalization of oxLDL and LOX-1 may be of pathophysiological significance, leading to a conceptual shift in understanding of the functional significance of AT1 internalization beyond its role in receptor desensitization. Taken together, these findings explain the difference in physiological and pathophysiological consequences of AT1 activation induced by oxLDL and Ang II.

AT1-induced activation of β-arrestin has been conventionally detected using a bioluminescent resonance energy transfer (BRET) assay. In the present study, we attempted to detect the oxLDL-induced BRET between AT1-Rluc8 and β-arrestin 2 (ARRB2)-mVenus in CHO-K1 cells in the presence of LOX-1. However, this trial failed because the oxLDL solution substantially attenuated the luminescence, resulting in oxLDL-induced elevation of the BRET ratio even in the absence of β-arrestin (ARRB)-mVenus (Figure S11). Instead, the signatures of LOX-1-AT1-dependent β-arrestin activation were observed by the detection of the molecular dynamics of LOX-1 on the cellular membrane in high-resolution live cell imaging (Figures 4A–4C). Given the observation that some merged puncta of AT1 and LOX-1 disappeared after the application of oxLDL, we conducted a quantitative analysis to detect intracellular trafficking of LOX-1 in response to oxLDL. While time-dependent changes in LOX-1 puncta could be a reflection of both its appearance and disappearance from the cellular membrane, a substantial decline in LOX-1 puncta in response to oxLDL was observed in parallel with the ability of AT1 to activate arrestin signaling.

Finally, endocytotic internalization of oxLDL was shown by the sublocalization of oxLDL through endosomes to lysosomes (Figures S1 and 5). This pathway was AT1-arrestin dependent as shown by microscopy analysis in which the cellular contents of fluorescent oxLDL were prominently attenuated by the ablation of the arrestin pathway of AT1 (Figure 4). Altogether, these findings establish a transport mechanism whereby the oxLDL-LOX-1-AT1 complex is internalized in cells via the β-arrestin-dependent endocytosis of AT1. It should be noted that LOX-1-dependent uptake of oxLDL involved an AT1-arrestin-independent pathway, as higher concentrations of oxLDL (10 μg/mL) increased the cellular content of oxLDL in CHO-LOX-1, which was not altered by DN β-arrestin (Figures 5C and S3). This finding is consistent with those of a previous study showing that LOX-1 alone or oxLDL binding to LOX-1 (10 μg/mL) undergoes ligand-independent constitutive internalization depending on its cytoplasmic tripeptide motif (Murphy et al., 2008). Indeed, 10 μg/mL oxLDL did not alter the dynamics of membrane LOX-1 in cells overexpressing LOX-1 alone, suggesting that the internalization of LOX-1 at this concentration involves a ligand-independent pathway (Figure 4). The observation of this LOX-1- and AT1-independent endocytic pathway is consistent with the study by Murphy et al. (2008), in which siRNA targeting *CHC17* did not inhibit the uptake of oxLDL in HeLa cells overexpressing LOX-1 alone. The existence of clathrin-independent endocytosis was also supported by the finding that loss of function of caveolae or clathrin inhibited the uptake of oxLDL in endothelial cells (Figure 6H). Nevertheless, it is conceivable that the AT1-independent endocytosis of the LOX-1-oxLDL complex is additive but not competitive with AT1-dependent endocytosis, as uptake of 10 μg/mL oxLDL was higher in CHO-LOX-1-AT1 than in CHO-LOX-1 (Figure 5C).

The question here is how oxLDL binding to LOX-1 stimulates such biased activation of AT1. AT1 forms a heterodimer with other GPCRs, and heterodimers tend to change the G protein preference and β-arrestin binding affinity (Barki-Harrington et al., 2003; Bellot et al., 2015; Nishimura et al., 2016; Quitterer et al., 2019; Rozenfeld et al., 2011; Siddiquee et al., 2013). However, while the known heterodimers of AT1 affect the signaling patterns of AT1 activation induced by its orthosteric ligand Ang II, there is no precedence of our finding that a receptor utilizes the adjacent GPCR as a mediator of signal transduction and a transporter of its ligand. Nevertheless, some clues for potential mechanisms have been provided by recent advances in characterizing biased AT1 activation by various stimuli. SII is a well-known biased agonist of AT1 that selectively activates β-arrestin, but recent findings have revealed its potential to activate G protein as well (Domazet et al., 2015; Sauliere et al., 2012). More recently, various Ang II analogs, including SII, were tested for the selectivity of G protein activation and β-arrestin signaling, and most of the analogs induced bias responses of AT1 against Gαq in favor of Gαi, Gα12, and β-arrestin (Namkung et al., 2018). AT1 is activated by mechanical stretch (Zou et al., 2004), and this activation is selective (Rakesh et al., 2010; Tang et al., 2014). Interestingly, Wang et al. (2018) recently reported that the mechanical stretch of AT1 activates Gαi but not Gq, which then mediates β-arrestin biased signaling. This Gαi-dependent activation of β-arrestin signaling is distinct from the current finding that β-arrestin signaling by oxLDL is not altered by the impaired ability of AT1 to activate G protein. However, the preference to activate Gαi compared to Gq appears to be consistent among various allosteric stimulators of AT1. Previous studies have suggested that the distinct signaling pathway of AT1 induced by different ligands depends on the ligand-specific structural change of the receptor. There are four crystal structures for inactive or active forms of AT1 reported in the Protein Data Bank (Clement et al., 2005; Quitterer et al., 2019; Zhang et al., 2015a, 2015b). Interestingly, recent structural analysis using double electron-electron resonance spectroscopy indicated that β-arrestin biased agonists induce less "open" conformational changes in AT1 than Ang II or agonists with enhanced Gαq coupling (Wingler et al., 2019). Further investigation is required to reveal the structural switch of AT1 induced by oxLDL binding to LOX-1, leading to a similar biased signaling pathway prevalent across diverse stimuli.

Interestingly, we found that pharmacological inhibition of AT1 by ARBs did not alter the β-arrestin-dependent internalization of the oxLDL-LOX-1-AT1 complex. This is in contrast to our previous findings that G-protein-dependent signaling of oxLDL-induced AT1 activation is inhibited by ARBs (Yamamoto et al., 2015). The concept of ARBs to inhibit oxLDL-LOX-1-induced AT1 activation is theoretically similar to that of "inverse agonist" potential of ARBs to inhibit constitutive activation of AT1 induced by mechanical stretch (Takezako et al., 2015). It is conceivable that the impact of ARBs on the oxLDL-LOX-1-induced structural change of AT1 is sufficient to block the G-protein-dependent pathway but insufficient to block the β-arrestin-dependent pathway. Further investigation is required to clarify the structural basis of the selectivity of ARBs in inhibiting oxLDL-induced AT1 activation.

We have demonstrated that a mechanism involving AT1 and β-arrestin can influence the uptake of oxLDL in human vascular endothelial cells; however, the pathophysiological significance of this phenomenon remains to be fully determined. We found that co-localization of oxLDL with lysosomes increased over time after endocytosis in cells expressing both AT1 and LOX-1, suggesting that the majority of oxLDL is terminally cleared from cells (Figures S1 and 5). This pathway is clearly distinct from the transcytosis of oxLDL, which was recently found to depend on SR-BI (Figure 6C) (Huang et al., 2019). We previously reported that oxLDL-induced endothelial dysfunction of the aortic ring was inhibited by ARB, as well as genetic deletion of *AT1a* in mice (Yamamoto et al., 2015). Therefore, although we found that the ERK1/2 activation induced by oxLDL was partially blocked upon inhibition of β-arrestin (Figure S8), it is conceivable that β-arrestin-dependent accumulation of oxLDL does not primarily contribute to endothelial dysfunction in normal tissues. Indeed, we found that the oxLDL-induced inflammatory response detected by the activation of NfκB depended on G protein signaling but not on β-arrestin signaling of AT1 (Figure 3A). Nevertheless, recent studies have suggested that the disruption of the endothelial autophagy-lysosomal pathway enhances the development of atherosclerosis, and oxLDL induces lysosomal dysfunction (Emanuel et al., 2014; Torisu et al., 2016; Vion et al., 2017). Further investigation is required to elucidate how far the endothelial uptake of oxLDL via the AT1-LOX-1 pathway contributes to the development of atherosclerosis *in vivo*. Additionally, LOX-1 belongs to the c-type lectin receptor family and functions as a pattern recognition receptor (PRR) that binds to multiple ligands, primarily including damage-associated molecular patterns and pathogen-associated molecular patterns (Miller et al., 2011). LOX-1 binds to multiple ligands besides oxLDL, including C-reactive protein, modified high-density lipoprotein, and remnant lipoprotein, all of which could promote atherosclerosis (Besler et al., 2011; Fujita et al., 2009; Shin et al., 2004).

Local production of Ang II may also promote atherosclerosis (Brasier et al., 2002). It has been shown that the development of atherosclerosis is attenuated by the genetic deletion of either AT1 (Daugherty et al., 2004; Wassmann et al., 2004) or LOX-1 (Mehta et al., 2007) in atherogenic mice. However, since our findings imply that multiple molecules share the same LOX-1-AT1 system to exert their roles in atherogenesis, it is difficult to determine how these individual molecules utilize the system and, thus, contribute to disease progression. In addition, it is of interest to clarify which pathways are more important in the development of atherosclerosis: G-protein-dependent induction of vascular damage or β-arrestin-dependent vascular accumulation of LOX-1 ligands. This is important from a therapeutic point of view, given the inhibitory effect of ARBs in the AT1-G protein-dependent pathway but not in the β-arrestin-dependent pathway. It also remains to be determined whether these distinct molecular pathways can synergistically contribute to the development of atherosclerosis. Finally, it is important to elucidate whether the canonical Ang II signaling pathway is affected by oxLDL-induced AT1 activation, and vice versa, because Ang II and oxLDL utilize the same receptor to trigger biological reactions *in vivo*. Indeed, we found the contrast cellular response by the combined treatment of Ang II with oxLDL in different assays and cell types. While we found that the combined treatment of Ang II and oxLDL prominently enhanced NfκB activity in CHO-LOX-1-AT1 (Figure 3B), the combined treatment of these ligands did not enhance the activation of ERK 1/2 compared to each treatment alone in endothelial cells (Figure S9). These results suggest that the combination of Ang II-AT1 signaling and oxLDL-LOX-1-AT1 signaling could exert either inhibitory or additive cellular response depending on undefined factors. The net cellular reaction in a milieu with the co-presence of Ang II and oxLDL can be influenced by many factors including the concentration of these ligands, the abundance of the receptors, and cell types. Further investigation using specific animal models is required to clarify these questions and understand the overall pathophysiological relevance of this molecular machinery.

In conclusion, we demonstrated the first example of a transport system whereby a PRR ligand stimulates biased signaling pathways of GPCR, which consequently leads to intracellular trafficking of the ligand. Given the ability of PRRs to capture diverse ligands and their physiological and pathophysiological significance, it will be of interest to determine the extent to which our findings regarding LOX-1 pertain to other PRRs and to evaluate the importance of these findings in health and disease.

Limitations of the study

Here, we use CHO cells, HUVECs, and HAECs. We have not yet analyzed the pathophysiological mechanisms *in vivo*.

Resource availability

Lead contact

Further information and requests for resources and reagents should be directed to and will be fulfilled by the lead contact, Koichi Yamamoto kyamamoto@geriat.med.osaka-u.ac.jp.

Material availability

This study did not include any new unique reagents, and all reagents generated in this study are available from the lead contact without restriction.

Data and code availability

The data sets supporting the current study are available from the lead contact upon reasonable request.

METHODS

All methods can be found in the accompanying Transparent methods supplemental file.

SUPPLEMENTAL INFORMATION

Supplemental information can be found online at https://doi.org/10.1016/j.isci.2021.102076.

REFERENCES

Barki-Harrington, L., Luttrell, L.M., and Rockman, H.A. (2003). Dual inhibition of beta-adrenergic and angiotensin II receptors by a single antagonist: a functional role for receptor-receptor interaction in vivo. Circulation 108, 1611–1618.

Beautrait, A., Paradis, J.S., Zimmerman, B., Giubilaro, J., Nikolajev, L., Armando, S., Kobayashi, H., Yamani, L., Namkung, Y., Heydenreich, F.M., et al. (2017). A new inhibitor of the beta-arrestin/AP2 endocytic complex reveals interplay between GPCR internalization and signalling. Nat. Commun. 8, 15054.

Bellot, M., Galandrin, S., Boularan, C., Matthies, H.J., Despas, F., Denis, C., Javitch, J., Mazeres, S., Sanni, S.J., Pons, V., et al. (2015). Dual agonist occupancy of AT1-R-alpha2C-AR heterodimers results in atypical Gs-PKA signaling. Nat. Chem. Biol. 11, 271–279.

Berk, B.C. (1999). Angiotensin II signal transduction in vascular smooth muscle: pathways activated by specific tyrosine kinases. J. Am. Soc. Nephrol. 10 (Suppl 11), S62–S68.

Besler, C., Heinrich, K., Rohrer, L., Doerries, C., Riwanto, M., Shih, D.M., Chroni, A., Yonekawa, K., Stein, S., Schaefer, N., et al. (2011). Mechanisms underlying adverse effects of HDL on eNOS-activating pathways in patients with coronary artery disease. J. Clin. Invest. 121, 2693–2708.

Brasier, A.R., Recinos, A., 3rd, and Eledrisi, M.S. (2002). Vascular inflammation and the renin-angiotensin system. Arterioscler Thromb. Vasc. Biol. 22, 1257–1266.

Clement, M., Martin, S.S., Beaulieu, M.E., Chamberland, C., Lavigne, P., Leduc, R., Guillemette, G., and Escher, E. (2005). Determining the environment of the ligand binding pocket of the human angiotensin II type I (hAT1) receptor using the methionine proximity assay. J. Biol. Chem. 280, 27121–27129.

Daugherty, A., Rateri, D.L., Lu, H., Inagami, T., and Cassis, L.A. (2004). Hypercholesterolemia stimulates angiotensin peptide synthesis and contributes to atherosclerosis through the AT1A receptor. Circulation 110, 3849–3857.

Domazet, I., Holleran, B.J., Richard, A., Vandenberghe, C., Lavigne, P., Escher, E., Leduc, R., and Guillemette, G. (2015). Characterization of angiotensin II molecular determinants involved in AT1 receptor functional selectivity. Mol. Pharmacol. 87, 982–995.

Emanuel, R., Sergin, I., Bhattacharya, S., Turner, J., Epelman, S., Settembre, C., Diwan, A., Ballabio, A., and Razani, B. (2014). Induction of lysosomal biogenesis in atherosclerotic macrophages can rescue lipid-induced lysosomal dysfunction and downstream sequelae. Arterioscler Thromb. Vasc. Biol. 34, 1942–1952.

Ferre, S., Casado, V., Devi, L.A., Filizola, M., Jockers, R., Lohse, M.J., Milligan, G., Pin, J.P., and Guitart, X. (2014). G protein-coupled receptor oligomerization revisited: functional and pharmacological perspectives. Pharmacol. Rev. 66, 413–434.

Forrester, S.J., Booz, G.W., Sigmund, C.D., Coffman, T.M., Kawai, T., Rizzo, V., Scalia, R., and Eguchi, S. (2018). Angiotensin II signal transduction: an update on mechanisms of physiology and pathophysiology. Physiol. Rev. 98, 1627–1738.

Fujita, Y., Kakino, A., Nishimichi, N., Yamaguchi, S., Sato, Y., Machida, S., Cominacini, L., Delneste, Y., Matsuda, H., and Sawamura, T. (2009). Oxidized LDL receptor LOX-1 binds to C-reactive protein and mediates its vascular effects. Clin. Chem. 55, 285–294.

Gentry, P.R., Sexton, P.M., and Christopoulos, A. (2015). Novel allosteric modulators of G protein-coupled receptors. J. Biol. Chem. 290, 19478–19488.

Grisanti, L.A., Schumacher, S.M., Tilley, D.G., and Koch, W.J. (2018). Designer approaches for G protein-coupled receptor modulation for cardiovascular disease. JACC Basic Transl Sci. 3, 550–562.

Haendeler, J., Ishida, M., Hunyady, L., and Berk, B.C. (2000). The third cytoplasmic loop of the angiotensin II type 1 receptor exerts differential effects on extracellular signal-regulated kinase (ERK1/ERK2) and apoptosis via Ras- and Rap1-dependent pathways. Circ. Res. 86, 729–736.

Hermosilla, T., Encina, M., Morales, D., Moreno, C., Conejeros, C., Alfaro-Valdes, H.M., Lagos-Meza, F., Simon, F., Altier, C., and Varela, D. (2017). Prolonged AT1R activation induces CaV1.2 channel internalization in rat cardiomyocytes. Sci. Rep. 7, 10131.

Huang, L., Chambliss, K.L., Gao, X., Yuhanna, I.S., Behling-Kelly, E., Bergaya, S., Ahmed, M., Michaely, P., Luby-Phelps, K., Darehshouri, A., et al. (2019). SR-B1 drives endothelial cell LDL transcytosis via DOCK4 to promote atherosclerosis. Nature 569, 565–569.

Hunyady, L. (1999). Molecular mechanisms of angiotensin II receptor internalization. J. Am. Soc. Nephrol. 10 (Suppl 11), S47–S56.

Hunyady, L., and Catt, K.J. (2006). Pleiotropic AT1 receptor signaling pathways mediating physiological and pathogenic actions of angiotensin II. Mol. Endocrinol. 20, 953–970.

Hunyady, L., Catt, K.J., Clark, A.J., and Gaborik, Z. (2000). Mechanisms and functions of AT(1) angiotensin receptor internalization. Regul. Pept. 91, 29–44.

Jean-Charles, P.Y., Kaur, S., and Shenoy, S.K. (2017). G protein-coupled receptor signaling through beta-arrestin-dependent mechanisms. J. Cardiovasc. Pharmacol. 70, 142–158.

Kang, D.S., Kern, R.C., Puthenveedu, M.A., von Zastrow, M., Williams, J.C., and Benovic, J.L. (2009). Structure of an arrestin2-clathrin complex reveals a novel clathrin binding domain that modulates receptor trafficking. J. Biol. Chem. 284, 29860–29872.

Khoury, E., Clement, S., and Laporte, S.A. (2014). Allosteric and biased g protein-coupled receptor signaling regulation: potentials for new therapeutics. Front. Endocrinol. (Lausanne) 5, 68.

Kim, J., Ahn, S., Ren, X.R., Whalen, E.J., Reiter, E., Wei, H., and Lefkowitz, R.J. (2005). Functional antagonism of different G protein-coupled receptor kinases for beta-arrestin-mediated angiotensin II receptor signaling. Proc. Natl. Acad. Sci. U S A. 102, 1442–1447.

Kita, T., Kume, N., Minami, M., Hayashida, K., Murayama, T., Sano, H., Moriwaki, H., Kataoka,

H., Nishi, E., Horiuchi, H., et al. (2001). Role of oxidized LDL in atherosclerosis. Ann. N. Y Acad. Sci. 947, 199–205, discussion 205-196.

Krupnick, J.G., Santini, F., Gagnon, A.W., Keen, J.H., and Benovic, J.L. (1997). Modulation of the arrestin-clathrin interaction in cells. Characterization of beta-arrestin dominant-negative mutants. J. Biol. Chem. 272, 32507–32512.

Lee, M.H., El-Shewy, H.M., Luttrell, D.K., and Luttrell, L.M. (2008). Role of beta-arrestin-mediated desensitization and signaling in the control of angiotensin AT1a receptor-stimulated transcription. J. Biol. Chem. 283, 2088–2097.

Li, D., and Mehta, J.L. (2005). Oxidized LDL, a critical factor in atherogenesis. Cardiovasc. Res. 68, 353–354.

Mehta, J.L., Chen, J., Hermonat, P.L., Romeo, F., and Novelli, G. (2006). Lectin-like, oxidized low-density lipoprotein receptor-1 (LOX-1): a critical player in the development of atherosclerosis and related disorders. Cardiovasc. Res. 69, 36–45.

Mehta, J.L., Sanada, N., Hu, C.P., Chen, J., Dandapat, A., Sugawara, F., Satoh, H., Inoue, K., Kawase, Y., Jishage, K., et al. (2007). Deletion of LOX-1 reduces atherogenesis in LDLR knockout mice fed high cholesterol diet. Circ. Res. 100, 1634–1642.

Miller, Y.I., Choi, S.H., Wiesner, P., Fang, L., Harkewicz, R., Hartvigsen, K., Boullier, A., Gonen, A., Diehl, C.J., Que, X., et al. (2011). Oxidation-specific epitopes are danger-associated molecular patterns recognized by pattern recognition receptors of innate immunity. Circ. Res. 108, 235–248.

Murphy, J.E., Vohra, R.S., Dunn, S., Holloway, Z.G., Monaco, A.P., Homer-Vanniasinkam, S., Walker, J.H., and Ponnambalam, S. (2008). Oxidised LDL internalisation by the LOX-1 scavenger receptor is dependent on a novel cytoplasmic motif and is regulated by dynamin-2. J. Cell Sci. 121, 2136–2147.

Namkung, Y., LeGouill, C., Kumar, S., Cao, Y., Teixeira, L.B., Lukasheva, V., Giubilaro, J., Simoes, S.C., Longpre, J.M., Devost, D., et al. (2018). Functional selectivity profiling of the angiotensin II type 1 receptor using pathway-wide BRET signaling sensors. Sci. Signal. 11.

Nishimura, A., Sunggip, C., Tozaki-Saitoh, H., Shimauchi, T., Numaga-Tomita, T., Hirano, K., Ide, T., Boeynaems, J.M., Kurose, H., Tsuda, M., et al. (2016). Purinergic P2Y6 receptors heterodimerize with angiotensin AT1 receptors to promote angiotensin II-induced hypertension. Sci. Signal. 9, ra7.

Oppermann, M., Freedman, N.J., Alexander, R.W., and Lefkowitz, R.J. (1996). Phosphorylation of the type 1A angiotensin II receptor by G protein-coupled receptor kinases and protein kinase C. J. Biol. Chem. 271, 13266–13272.

Qian, H., Pipolo, L., and Thomas, W.G. (2001). Association of beta-Arrestin 1 with the type 1A angiotensin II receptor involves phosphorylation of the receptor carboxyl terminus and correlates with receptor internalization. Mol. Endocrinol. 15, 1706–1719.

Quitterer, U., Fu, X., Pohl, A., Bayoumy, K.M., Langer, A., and AbdAlla, S. (2019). Beta-Arrestin1 prevents preeclampsia by downregulation of mechanosensitive AT1-B2 receptor Heteromers. Cell 176, 318–333 e319.

Rakesh, K., Yoo, B., Kim, I.M., Salazar, N., Kim, K.S., and Rockman, H.A. (2010). beta-Arrestin-biased agonism of the angiotensin receptor induced by mechanical stress. Sci. Signal. 3, ra46.

Ranjan, R., Dwivedi, H., Baidya, M., Kumar, M., and Shukla, A.K. (2017). Novel structural insights into GPCR-beta-arrestin interaction and signaling. Trends Cell Biol. 27, 851–862.

Rozenfeld, R., Gupta, A., Gagnidze, K., Lim, M.P., Gomes, I., Lee-Ramos, D., Nieto, N., and Devi, L.A. (2011). AT1R-CB(1)R heteromerization reveals a new mechanism for the pathogenic properties of angiotensin II. EMBO J. 30, 2350–2363.

Santos, R., Ursu, O., Gaulton, A., Bento, A.P., Donadi, R.S., Bologa, C.G., Karlsson, A., Al-Lazikani, B., Hersey, A., Oprea, T.I., et al. (2017). A comprehensive map of molecular drug targets. Nat. Rev. Drug Discov. 16, 19–34.

Sato, P.Y., Chuprun, J.K., Schwartz, M., and Koch, W.J. (2015). The evolving impact of g protein-coupled receptor kinases in cardiac health and disease. Physiol. Rev. 95, 377–404.

Sauliere, A., Bellot, M., Paris, H., Denis, C., Finana, F., Hansen, J.T., Altie, M.F., Seguelas, M.H., Pathak, A., Hansen, J.L., et al. (2012). Deciphering biased-agonism complexity reveals a new active AT1 receptor entity. Nat. Chem. Biol. 8, 622–630.

Shenoy, S.K., and Lefkowitz, R.J. (2011). beta-Arrestin-mediated receptor trafficking and signal transduction. Trends Pharmacol. Sci. 32, 521–533.

Shin, H.K., Kim, Y.K., Kim, K.Y., Lee, J.H., and Hong, K.W. (2004). Remnant lipoprotein particles induce apoptosis in endothelial cells by NAD(P)H oxidase-mediated production of superoxide and cytokines via lectin-like oxidized low-density lipoprotein receptor-1 activation: prevention by cilostazol. Circulation 109, 1022–1028.

Shukla, A.K., Kim, J., Ahn, S., Xiao, K., Shenoy, S.K., Liedtke, W., and Lefkowitz, R.J. (2010). Arresting a transient receptor potential (TRP) channel: beta-arrestin 1 mediates ubiquitination and functional down-regulation of TRPV4. J. Biol. Chem. 285, 30115–30125.

Siddiquee, K., Hampton, J., McAnally, D., May, L., and Smith, L. (2013). The apelin receptor inhibits the angiotensin II type 1 receptor via allosteric trans-inhibition. Br. J. Pharmacol. 168, 1104–1117.

Smith, J.S., and Rajagopal, S. (2016). The beta-arrestins: multifunctional regulators of G protein-coupled receptors. J. Biol. Chem. 291, 8969–8977.

Steinberg, D. (1997). Low density lipoprotein oxidation and its pathobiological significance. J. Biol. Chem. 272, 20963–20966.

Steinberg, D., and Witztum, J.L. (2010). Oxidized low-density lipoprotein and atherosclerosis. Arterioscler Thromb. Vasc. Biol. 30, 2311–2316.

Sun, S.W., Zu, X.Y., Tuo, Q.H., Chen, L.X., Lei, X.Y., Li, K., Tang, C.K., and Liao, D.F. (2010). Caveolae

and caveolin-1 mediate endocytosis and transcytosis of oxidized low density lipoprotein in endothelial cells. Acta Pharmacol. Sin 31, 1336–1342.

Takezako, T., Unal, H., Karnik, S.S., and Node, K. (2015). Structure-function basis of attenuated inverse agonism of angiotensin II type 1 receptor blockers for active-state angiotensin II type 1 receptor. Mol. Pharmacol. 88, 488–501.

Tang, W., Strachan, R.T., Lefkowitz, R.J., and Rockman, H.A. (2014). Allosteric modulation of beta-arrestin-biased angiotensin II type 1 receptor signaling by membrane stretch. J. Biol. Chem. 289, 28271–28283.

Torisu, K., Singh, K.K., Torisu, T., Lovren, F., Liu, J., Pan, Y., Quan, A., Ramadan, A., Al-Omran, M., Pankova, N., et al. (2016). Intact endothelial autophagy is required to maintain vascular lipid homeostasis. Aging Cell 15, 187–191.

Toshima, S., Hasegawa, A., Kurabayashi, M., Itabe, H., Takano, T., Sugano, J., Shimamura, K., Kimura, J., Michishita, I., Suzuki, T., et al. (2000). Circulating oxidized low density lipoprotein levels. A biochemical risk marker for coronary heart disease. Arterioscler Thromb. Vasc. Biol. 20, 2243–2247.

Turu, G., Szidonya, L., Gaborik, Z., Buday, L., Spat, A., Clark, A.J., and Hunyady, L. (2006). Differential beta-arrestin binding of AT1 and AT2 angiotensin receptors. FEBS Lett. 580, 41–45.

Violin, J.D., and Lefkowitz, R.J. (2007). Beta-arrestin-biased ligands at seven-transmembrane receptors. Trends Pharmacol. Sci. 28, 416–422.

Vion, A.C., Kheloufi, M., Hammoutene, A., Poisson, J., Lasselin, J., Devue, C., Pic, I., Dupont, N., Busse, J., Stark, K., et al. (2017). Autophagy is required for endothelial cell alignment and atheroprotection under physiological blood flow. Proc. Natl. Acad. Sci. U S A 114, E8675–E8684.

Wang, J., Hanada, K., Gareri, C., and Rockman, H.A. (2018). Mechanoactivation of the angiotensin II type 1 receptor induces beta-arrestin-biased signaling through Galphai coupling. J. Cell Biochem. 119, 3586–3597.

Wassmann, S., Czech, T., van Eickels, M., Fleming, I., Bohm, M., and Nickenig, G. (2004). Inhibition of diet-induced atherosclerosis and endothelial dysfunction in apolipoprotein E/angiotensin II type 1A receptor double-knockout mice. Circulation 110, 3062–3067.

Wingler, L.M., Elgeti, M., Hilger, D., Latorraca, N.R., Lerch, M.T., Staus, D.P., Dror, R.O., Kobilka, B.K., Hubbell, W.L., and Lefkowitz, R.J. (2019). Angiotensin analogs with divergent bias stabilize distinct receptor conformations. Cell 176, 468–478 e411.

Wootten, D., Christopoulos, A., and Sexton, P.M. (2013). Emerging paradigms in GPCR allostery: implications for drug discovery. Nat. Rev. Drug Discov. 12, 630–644.

Yamamoto, K., Kakino, A., Takeshita, H., Hayashi, N., Li, L., Nakano, A., Hanasaki-Yamamoto, H., Fujita, Y., Imaizumi, Y., Toyama-Yokoyama, S., et al. (2015). Oxidized LDL (oxLDL) activates the angiotensin II type 1 receptor by binding to the lectin-like oxLDL receptor. FASEB J. 29, 3342–3356.

Zhang, H., Unal, H., Desnoyer, R., Han, G.W., Patel, N., Katritch, V., Karnik, S.S., Cherezov, V., and Stevens, R.C. (2015a). Structural basis for ligand recognition and functional selectivity at angiotensin receptor. J. Biol. Chem. *290*, 29127–29139.

Zhang, H., Unal, H., Gati, C., Han, G.W., Liu, W., Zatsepin, N.A., James, D., Wang, D., Nelson, G., Weierstall, U., et al. (2015b). Structure of the Angiotensin receptor revealed by serial femtosecond crystallography. Cell *161*, 833–844.

Zou, Y., Akazawa, H., Qin, Y., Sano, M., Takano, H., Minamino, T., Makita, N., Iwanaga, K., Zhu, W., Kudoh, S., et al. (2004). Mechanical stress activates angiotensin II type 1 receptor without the involvement of angiotensin II. Nat. Cell Biol. 6, 499–506.

Supplemental Information

The endocytosis of oxidized LDL

via the activation of the angiotensin II

type 1 receptor

Toshimasa Takahashi, Yibin Huang, Koichi Yamamoto, Go Hamano, Akemi Kakino, Fei Kang, Yuki Imaizumi, Hikari Takeshita, Yoichi Nozato, Satoko Nozato, Serina Yokoyama, Motonori Nagasawa, Tatsuo Kawai, Masao Takeda, Taku Fujimoto, Kazuhiro Hongyo, Futoshi Nakagami, Hiroshi Akasaka, Yoichi Takami, Yasushi Takeya, Ken Sugimoto, Herbert Y. Gaisano, Tatsuya Sawamura, and Hiromi Rakugi

1   **Transparent Methods**

2   **Cell culture and materials**

3   HUVECs and HAECs were cultured in EGM-2 (Clontech, USA). Cells less than five

4   passages were used for the experiments. Transgenic CHO cells were maintained in F-12

5   Nutrient Mixture with Glutamax^{TM}-I (Thermo Fisher Scientific, USA), 10% fetal bovine

6   serum (FBS), and appropriate selection reagents as described below. Transcription of the

7   genes in transgenic CHO cells was induced by adding doxycycline into culture media for

8   24 h at a final concentration of 300 ng/ml. CHO-K1 cells were maintained in F-12

9   Nutrient Mixture with Glutamax^{TM}-I (Thermo Fisher Scientific, USA) and 10% FBS.

10   barbadin was purchased from Toronto research chemicals (Canada). Losartan, telmisartan,

11   and irbesartan were purchased from Cayman Chemical (USA).

12

13   **Construction of plasmid vectors**

14   For stable transformants, pTRE2hyg vector encoding mutated human AT1 with impaired

15   ability to activate G protein (pTRE2hyg-HA-FLAG-hAT1mβ) and pTRE2hyg vector

16   (Clontech, USA) encoding mutated hAT1 with impaired ability to activate β-arrestin

17   (pTRE2hyg-HA-FLAG-hAT1mg) were created using site direct mutagenesis. Briefly,

18   pTRE2hyg-HA-FLAG-hAT1mβ was created using a primeSTAR mutagenesis basal kit

19   (Takara, Japan) to delete amino acids 221 and 222 from the pTRE2hyg vector encoding

20   hAT1 tagged with signal peptide-HA-FLAG at the N-terminus (pTRE2hyg-HA-FLAG-

21   hAT1) (Haendeler et al., 2000; Yamamoto et al., 2015). pTRE2hyg-HA-FLAG-hAT1mg

22   was created using a KOD-plus mutagenesis kit (Toyobo, Japan) to substitute amino acids

23   at the carboxyl terminus (Thr (332), Ser (335), Thr (336), Ser (338)) into alanine from

24   pTRE2hyg-HA-FLAG-hAT1 (Qian et al., 2001). For the BRET assay, human β-arrestin

25   2 was subcloned into mVenus N1 (Plasmid #27793, Addgene). Expression vectors for

26   LOX-1 and Dectin-1 were created as shown in a previous study (Yamamoto et al., 2015).

27   For real-time imaging, LOX-1 tagged with V5-6×His at the C-terminus (V5-LOX-1) was

28   subcloned into pmScarlet_C1 (Plasmid #85042, Addgene) (mScarlet-LOX-1). HA-

29   FLAG-hAT1, HA-FLAG-hAT1mβ, and HA-FLAG-hAT1mg were subcloned into

30   pcDNA3-EGFP (Plasmid #85042, Addgene) (AT1-GFP, AT1mg-GFP, and AT1mβ-GFP).

31   Plasmid encoding dominant-negative β-arrestin was created by subcloning the clathrin-

32   binding domain of β-arrestin (β-arrestin (319–418)) into the pTRE2hyg vector (DN-

33   βarrestin) (Krupnick et al., 1997). Negative control vector of DN-β-arrestin was created

34   using primeSTAR mutagenesis basal kit to delete the clathrin binding box domain

35   (LIELD) from DN-β-arrestin (Kang et al., 2009).

36

37   **Stable transformants**

38   CHO-K1 cells expressing tetracycline-inducible human LOX-1 tagged with V5-6×His at

39   C-terminus (CHO-LOX-1), cells expressing human HA-FLAG-hAT1 (CHO-AT1), and

40   cells expressing both human LOX-1 and AT1 (CHO-LOX-1-AT1) were maintained as

41   previously described (Fujita et al., 2009; Yamamoto et al., 2015). To establish cells

42   expressing both LOX-1 and mutated AT1, pTRE2hyg-HA-FLAG-hAT1mβ or

43   pTRE2hyg-HA-FLAG-hAT1mg were co-transfected with pSV2bsr vector (Funakoshi,

44   Japan) into CHO-LOX-1 using Lipofectamin2000 transfection reagent (Thermo Fisher

45   Scientific, USA). The stable transformants were selected with 400 μg/ml of hygromycin

46   B (Wako, Japan) and 10 μg/ml of blasticidin S (Funakoshi, Japan). The resistant clones

47   expressing LOX-1 and mutated AT1 in response to doxycycline (Calbiochem, USA) were

48   selected for use in experiments (CHO-LOX-1-AT1mg and CHO-LOX-1-AT1mβ).

49

Immunofluorescence staining

Tagged LOX-1 and AT1 (or mutated AT1) in genetically engineered CHO cells were

detected using mouse anti-V5 (Nacalai, Japan) and rat anti-FLAG (Novus Biologicals,

USA) antibodies in combination with rabbit Alexa488-conjugated anti-rat IgG and goat

Alexa594-conjugated anti-mouse IgG (Thermo Fisher Scientific, USA), respectively, as

reported previously (Yamamoto et al., 2015). Nuclei were counterstained with DAPI

(Sigma, USA). Images were acquired with a fluorescence microscope (BZ-X700,

Keyence, Japan).

Cell-based ELISA

Cells were seeded at 150,000 cells per well onto 96-well transparent cell culture plates

and incubated overnight at 37°C. The following day, cultures were transferred to serum-

free conditions and cells were further incubated for 24 h. Thereafter, cells were fixed by

4% paraformaldehyde without permeabilization, incubated with mouse anti-V5 or rat

anti-FLAG antibodies, then incubated with HRP-conjugated mouse or rat secondary

antibodies, respectively. TMB reagents (SeraCare Life Sciences, USA) were then added

to each well and the colorimetric reaction was stopped with stop solution (SeraCare Life

67 Sciences, USA). OD 450 values were measured using Multiskan Go (Thermo Fisher

68 Scientific, USA). Each measurement value was adjusted by subtracting the value of

69 negative control with secondary antibodies in the absence of first antibodies.

70

71

72 *In situ* **PLA**

73 *In situ* PLA was used to detect the proximity of LOX-1 with AT1 or mutated AT1 using

74 Duolink, from Olink Bioscience (Uppsala, Sweden), according to our previous study

75 (Yamamoto et al., 2015). Images were acquired using a fluorescence microscope (BZ-

76 X700, Keyence, Japan). Quantitative fluorescence cell image analysis was performed

77 using the BZ-X analyzer system (Keyence, Japan).

78

79 **Preparation of oxLDL and fluorescence-labelled oxLDL**

80 Human plasma LDL (1.019-1.063 g/ml) isolated by sequential ultracentrifugation was

81 oxidized using 20 μM $CuSO_4$ in PBS at 37°C for 24 h. Oxidation was terminated by

82 adding excess EDTA. Oxidation of LDL was analyzed using agarose gel electrophoresis

83 for migration versus LDL (Yamamoto et al., 2015). Labeling of oxLDL with 1,1-

84 dioctadecyl-3,3,3,3-tetramethylindocarbocyanine perchlorate (DiI, Thermo Fisher

85   Scientific, USA) was performed as described previously (Yamamoto et al., 2015).

86

87   **Quantification of cellular cAMP content**

88   Gi-dependent inhibition of adenylyl cyclase activity was assessed by inhibition of

89   Forskolin-dependent cAMP production using a cAMP dynamic 2 kit (Cisbio, France).

90   Cells were seeded at 80,000 cells per well onto 96-well transparent cell culture plates and

91   incubated overnight at 37°C. The following day, cultures were transferred to serum-free

92   conditions and cells were further incubated for 24 h. Thereafter, cells were treated for 1

93   h with DMEM without phenol, 1 mM IBMX, and 1 µM Forskolin, including vehicle,

94   oxLDL, and AII at the indicated concentrations at 37°C, 5% CO_2. Triton X was then

95   added to a final concentration of 1% and cell lysates were prepared after shaking the

96   plates for 30 min. Finally, cell lysates were transferred to 384-well white plates and cAMP

97   levels were measured by incubation of cell lysates with FRET reagents (the cryptate-

98   labeled anti-cAMP antibody and the d2-labeled cAMP analogue) for 1 h at 37°C. The

99   emission signals were measured at 590 and 665 nm after excitation at 340 nm, using the

100   ARTEMIS plate reader (Furuno Electric Co. Ltd, Japan). The FRET ratio: F =

101   (fluorescence 665 nm/fluorescence 590 nm) $\times 10^4$ was transformed into cAMP

102   concentration by calculation using the four-parameter logistic curve of standard samples.

5

103   Measurement values were normalized to that of vehicle treatment.

104

105   **Quantification of cellular IP1 accumulation**

106   Gq-dependent activation of phospholipase C was quantified by measurement of IP1 using

107   the IP-One assay kit (Cisbio, France). Cells were seeded at 80,000 cells per well onto 96-

108   well transparent cell culture plates and incubated overnight at 37°C. The following day,

109   cultures were transferred to serum-free conditions and further incubated for 24 h.

110   Thereafter, cells were treated for 1 h with IP1 stimulation buffer mixed with the same

111   amount of DMEM without phenol, including vehicle, oxLDL, and AII at an indicated

112   concentration at 37°C, 5% CO_2. Triton X was then added to a final concentration of 1%,

113   and cell lysates were prepared after shaking the plates for 30 min. Finally, cell lysates

114   were transferred to a 384-well white plate and IP1 levels were measured by incubation of

115   cell lysates with FRET reagents (the cryptate-labeled anti-IP1 antibody and the d2-labeled

116   IP1 analogue) for 1 h at 37°C. The emission signals were measured at 590 and 665 nm

117   after excitation at 340 nm, using the ARTEMIS plate reader (Furuno Electric Co. Ltd.,

118   Japan). The FRET ratio: F= (fluorescence 665 nm/fluorescence 590 nm) $\times 10^4$ was

119   transformed into IP1 concentration by calculation using the four-parameter logistic curve

120   of standard samples. Measurement values were normalized to that of vehicle treatment.

121

Real-time imaging of dynamics in LOX-1 and AT1 on cellular membranes

Twenty-four hours before imaging experiments, CHO cells were transfected with LOX-

1-mScarlet and mock-GFP AT1-GFP or AT1 mutants-GFP by electroporation and seeded

in a 35 mm glass base dish (Iwaki, Japan) pre-coated with 1000X diluted 10 mg/ml Poly-

L-Lysine (ScienCell, USA) 1 h before seeding. The growth medium was replaced with

imaging buffer (pH 7.4) containing 125 mM NaCl, 5 mM KCl, 1.2 mM $MgCl_2$, 1.3 mM

$CaCl_2$, 25 mM HEPES, and 3 mM D-glucose with pH adjusted to 7.4 with NaOH.

Dynamic images of the cells were obtained at 25°C using SpinSR10 inverted spinning

disk-type confocal super-resolution microscope (Olympus, Japan) equipped with a 100x

NA1.49 objective lens (UAPON100XOTIRF, Olympus, Japan) and an ORCA-Flash 4.0

V2 scientific CMOS camera (Hamamatsu Photonics KK, Japan) at 5 s intervals. The

imaging experiment was performed with CellSens Dimension 1.11 software using 3D

deconvolution algorithm (Olympus, Japan).

135

Quantification of change in LOX-1 localization on cellular membrane

A count of puncta was performed using separated images visualizing LOX-1-scarlet just

before (0 min) and 3 min after ligand application. Puncta was manually counted by a

139   blinded observer, and number of puncta at 0 and 3 min was determined (N0 and N3,

140   respectively). Change in puncta was calculated as (N0-N3)/N0 (Fig 4a).

141

142   **Detection of membrane-bound oxLDL**

143   Genetically engineered CHO cells were treated for 30 min with Dil-labeled oxLDL at a

144   final concentration of 2 µg/ml on ice, as described previously (Yamamoto et al., 2015).

145   The cells were then washed twice and fixed with neutral buffered formalin. Nuclei were

146   stained with DAPI (1 µg/ml). Images were acquired using a fluorescence microscope

147   (BZ-X700, Keyence, Japan). Quantitative fluorescence cell image analysis was

148   performed using the BZ-X analyzer system (Keyence, Japan).

149

150   **Visualization of co-localization of oxLDL with endocytic organelles and lysosome**

151   CHO-LOX-1-AT1 cells and HUVECs were seeded in a 35 mm four well glass base dish

152   (Iwaki, Japan) pre-coated with 1000X diluted 10 mg/ml Poly-L-Lysine (ScienCell, USA)

153   1 h before seeding. The following day, cells were treated with CellLight® for early and

154   late endosomes and lysosomes, according to the instructions (Thermo Fisher Scientific,

155   USA). After 24 h, cells were treated for 30 min with Dil-labeled oxLDL at a concentration

156   of 2 µg/ml. The cells were then washed twice with cultured media and fixed with neutral

157   buffered formalin immediately or after 5 h incubation in a CO_2 incubator. Images were

158   obtained using a SpinSR10 inverted spinning disk-type confocal super-resolution

159   microscope (Olympus, Japan) equipped with a 100x NA1.49 objective lens

160   (UAPON100XOTIRF, Olympus, Japan) and an ORCA-Flash 4.0 V2 scientific CMOS

161   camera (Hamamatsu Photonics KK, Japan). The imaging experiment was performed with

162   the CellSens Dimension 1.11 software using 3D deconvolution algorithm (Olympus,

163   Japan).

164

165   **Detection of colocalization of endosomes or lysosomes with DiI-oxLDL**

166   Before determining sub-pixel localization of lysosomes and endosomes, obtained raw

167   images were processed by despeckle and à trous wavelet transform algorithm to reduce

168   noise and remove the background with Fiji. Using custom MATLAB software, the

169   weighted centroid sub-pixel localizations were detected automatically. We confirmed

170   these results point-by-point to remove any possible artifacts then quantified the

171   colocalizations. Based on the resolution limit and configuration of our microscope, we

172   defined a 300 nm radius as the cut-off of subpixel colocalization.

173

174

175 **Detection of intracellular oxLDL content**

176 Genetically engineered CHO cells seeded in 96-well plates were treated for 30 min with

177 Dil-labeled oxLDL at a concentration of 2 μg/ml unless otherwise indicated in a CO_2

178 incubator at 37°C. HUVECs and HAECs in 96-well plates were treated for the indicated

179 time duration (10min, 30min, or 6 h) with Dil-labeled oxLDL at a concentration of 2

180 μg/ml in a CO_2 incubator. The cells were then washed twice with cultured media and

181 further incubated overnight to wash out the membrane-bound oxLDL. The cells were then

182 washed twice and fixed with neutral buffered formalin. Nuclei were stained with DAPI

183 (1 μg/ml). Images were acquired using a fluorescence microscope (BZ-X700, Keyence,

184 Japan). Quantitative fluorescence cell image analysis was performed using the BZ-X

185 analyzer system (Keyence, Japan).

186

187 **Transfection of CHO cells with dominant negative β-arrestin**

188 Genetically engineered CHO cells were transfected with DN-β-arrestin or negative

189 control vector using Lipofectamin LTX & PLUS reagent (Thermo Fisher Scientific, USA),

190 according to the manufacturer's instructions. Treatment with Dil-oxLDL was performed

191 24 h after transfection.

192

Luciferase reporter assay

Cells were seeded in a 96-well plate and were cotransfected with 100 ng of a plasmid containing Firefly luciferase driven by the NF-κB binding site (Promega, USA), and 10 ng of pRL-CMV Renilla luciferase control reporter vector (Promega Corp., Madison, WI, USA) by using Lipofectamine LTX with PLUS reagent kit (Thermo Fisher Scientific). After being cultured for 6 hours, the cells were starved in 0.1 % FBS supplemented with 300 ng/mL doxycycline to induce LOX-1 expression for 24 hours. Then, oxLDL was added to cells and incubated for 24 hours. Cells were washed once with PBS and lysed by incubation with 150 μL Passive Lysis Buffer from the Dual-Luciferase Reporter Assay Kit (Promega) for 15 minutes at room temperature with mixing. Lysates (10 μL) were loaded onto a 96-well white plate, and firefly and Renilla luciferase activities were determined. Luminescence was measured by using a Spark® microplate reader (TECAN, Switzerland)

Transfection of human endothelial cells with siRNA

HUVECs and HAVSMCs were plated to be 50% confluent on the day of transfection. Silencer® select siRNA for LOX-1 and/or AT1 (Thermo Fisher Scientific, USA) was transfected into the cells in media without serum and antibiotics using lipofectamine

211   RNAiMAX (Thermo Fisher Scientific, USA), according to the manufacturer's

212   instructions. Treatment with Dil-oxLDL was performed 24 h after transfection.

213

214   **Quantitative real-time PCR**

215   Total RNA was extracted using an RNeasy Mini Kit (Thermo Fisher Scientific, USA)

216   with DNase I treatment, and an equivalent amount of RNA was transcribed to cDNA by

217   the RevetraAce qPCR RT kit (FSQ-101, TOYOBO, Japan). Quantitative real-time PCR

218   was performed and analyzed on a model 7900 sequence detector (Thermo Fisher

219   Scientific, USA) using TaqMan gene-expression assays for *LOX-1* (Hs01552593_m1)

220   and   *AT1*   (5'-ACGTGTCTCAGCATTGATCGAT-3'   and   5'-

221   GTCGAAGGCGGGACTTCA-3' for primers, and 5'-CCTGGCTATTGTTCACC-3' for

222   probe), or the SYBR green qPCR system (Thermo Fisher Scientific, USA) with specific

223   primer   pairs   for   *SCARB1*   (5'-CTGTGGGTGAGATCATGTGG-3'   and   5'-

224   GCCAGAAGTCAACCTTGCTC-3'), *ARRB1* (5'-GGAGAACCCATCAGCGTCAA-3'

225   and   5'-GGGCACTTGTACTGAGCTGT-3'),   *ARRB2*   *(5'-

226   CAACTCCACCAAGACCGTCAAGA-3'   and   5'-

227   TTCGAGTTGAGCCACAGGACACTT-3'), *GRK2* (5'-ATGCATGGCTACATGTCCA-

228   3' and 5'-ATCTCCTCCATGGTCAGCAG-3'),   *GRK3*   (5'-

229 AGCTGTAGAACACGTACAAAGTC-3' and 5'-ATGTCACCTCGAAGGCTTTCA-3'),

230 *GRK5* (5'-ACCTGAGGGGAGAACCATTC-3' and 5'-TGGACTCCCCTTTCCTCTTT-

231 3'), *GRK6* (5'-TAGCGAACACGGTGCTACTC-3' and 5'-

232 GCTGATGTGAGGGAACTGGA-3'), *CLTC* (5'-GCCAGATGTCGTCCTGGAAA-3'

233 and 5'-AGCTGGGGCTGACCATAAAC-3'), and *CAV1* (5'-

234 CCAAGGAGATCGACCTGGTCAA-3' and 5'-GCCGTCAAAACTGTGTGTCCCT-3')

235 The expression level of each gene was determined by the standard curve method and

236 normalized using *GAPDH* mRNA (5'-GCCATCAATGACCCCTTCATT-3' and 5'-

237 TCTCGCTCCTGGAAGATGG-3') as an internal control.

238 **Detection of phosphorylation of ERK1/2**

239 Cells treated with oxLDL or vehicle were kept in an incubator at 37°C for 10 min.

240 Subsequently, cells were washed twice with PBS, and lysed using M-PER Mammalian

241 Protein Extraction Reagent (Thermo Scientific, Waltham, MA, USA) with protease

242 inhibitor and phosphatase inhibitor followed by Western blotting analysis as described

243 below.

244 **Western blotting analysis**

245 Proteins were separated by SDS-PAGE and electrophoretically transferred to

246 polyvinylidene fluoride membranes for Western blot analysis. The membranes were

247 blocked with 5% nonfat dried milk and incubated with primary antibodies overnight at

248 4ºC. The primary antibodies used in this study were anti–phospho-ERK1/2

249 (Thr202/Tyr204) antibody, anti–total-ERK1/2 antibody (Cell Signaling Technology,

250 Danvers, MA, USA). Bands were visualized using Chemi-Lumi One Super (Nacalai

251 Tesque). Densitometoric analysis was performed with chemiluminescence detection

252 system (LAS-4000 mini, GE Healthcare, Pittsburgh, PA, USA)

253

254 **Bioluminescence resonance energy transfer assay to monitor AT1-β-arrestin**

255 **interaction**

256 CHO-K1 cells were seeded onto a 35 mm dish at a density of 3×10^5 cells. The following

257 day, cells were transfected with AT1-rluc, β-arrestin2-mVenus, and non-fluorescence-

258 labelled LOX-1, or Dectin-1 of 0.9, 0.3, and 1.8 μg, respectively, using Lipofectamin

259 LTX & PLUS reagent (Thermo Fisher Scientific, USA), according to the manufacturer's

260 instructions. Cells were also transfected with AT1-rluc and non-fluorescence-labelled

261 Dectin-1 of 0.9 and 1.8 μg without β-arrestin2-mVenus. Cultures were transferred to

262 serum-free conditions after 24 h of transfection and further incubated for 24 h. Thereafter,

263 cells were prepared in white clear-bottom 96-well plates at a density of 100,000 cells per

264 well. Coelenterazine was added to each well at a final concentration of 5 μM and assays

265   were carried out immediately on a Spark® microplate reader (TECAN, Switzerland), and

266   the BRET ratio (emission mVenus/emission Rluc) was calculated. After 3 min of reading

267   of the baseline (the final baseline reading is presented at 0), cells were exposed to vehicle,

268   oxLDL (100 μg/ml), SII (10–5 M), or AII (10–5 M) for 10 min. The relative change in

269   intramolecular BRET ratio was calculated by subtracting the average BRET ratio

270   measured for cells stimulated with vehicle.

271

272   **Statistical analyses**

273   All data are presented as the mean ± SEM. Significant differences between two treatments

274   or among multiple treatments were determined by Student's t-test or one-way ANOVA

275   with Bonferroni testing, respectively.

276

277

278

279

280   **References**

281   Fujita, Y., Kakino, A., Nishimichi, N., Yamaguchi, S., Sato, Y., Machida, S., Cominacini, L.,
282   Delneste, Y., Matsuda, H., and Sawamura, T. (2009). Oxidized LDL receptor LOX-1 binds
283   to C-reactive protein and mediates its vascular effects. Clin Chem *55*, 285-294.
284   Haendeler, J., Ishida, M., Hunyady, L., and Berk, B.C. (2000). The third cytoplasmic loop of
285   the angiotensin II type 1 receptor exerts differential effects on extracellular signal-
286   regulated kinase (ERK1/ERK2) and apoptosis via Ras- and Rap1-dependent pathways. Circ

287   Res *86*, 729-736.

288   Kang, D.S., Kern, R.C., Puthenveedu, M.A., von Zastrow, M., Williams, J.C., and Benovic,

289   J.L. (2009). Structure of an arrestin2-clathrin complex reveals a novel clathrin binding

290   domain that modulates receptor trafficking. J Biol Chem *284*, 29860-29872.

291   Krupnick, J.G., Santini, F., Gagnon, A.W., Keen, J.H., and Benovic, J.L. (1997). Modulation

292   of the arrestin-clathrin interaction in cells. Characterization of beta-arrestin dominant-

293   negative mutants. J Biol Chem *272*, 32507-32512.

294   Qian, H., Pipolo, L., and Thomas, W.G. (2001). Association of beta-Arrestin 1 with the type

295   1A angiotensin II receptor involves phosphorylation of the receptor carboxyl terminus and

296   correlates with receptor internalization. Mol Endocrinol *15*, 1706-1719.

297   Yamamoto, K., Kakino, A., Takeshita, H., Hayashi, N., Li, L., Nakano, A., Hanasaki-

298   Yamamoto, H., Fujita, Y., Imaizumi, Y., Toyama-Yokoyama, S.*, et al.* (2015). Oxidized LDL

299   (oxLDL) activates the angiotensin II type 1 receptor by binding to the lectin-like oxLDL

300   receptor. FASEB J *29*, 3342-3356.

301
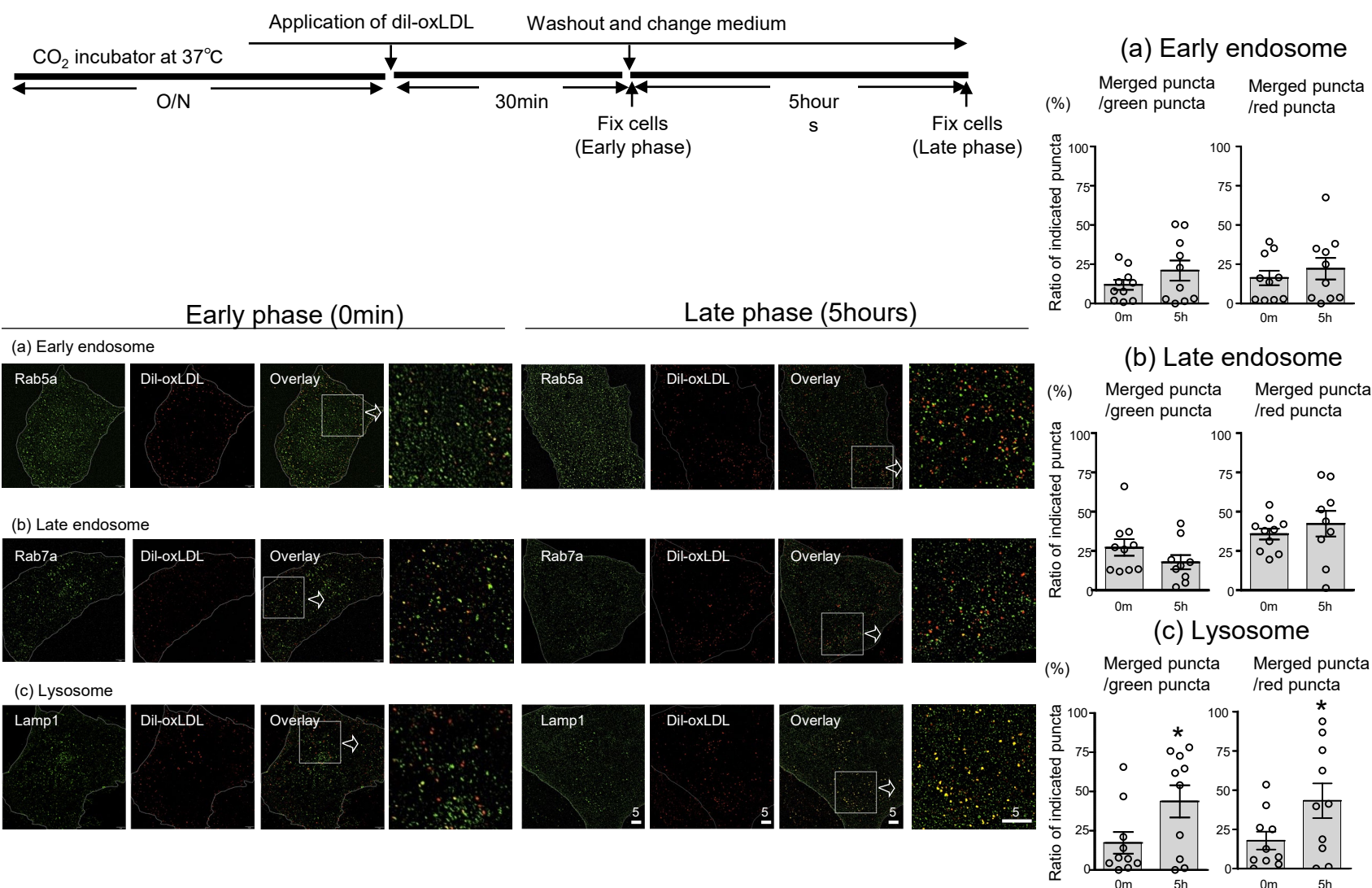
Figure S1: Endocytic traffic of oxLDL with early endosomes, late endosomes and lysosome in CHO. Related to Figure 5.

Visualization of co-localization of oxLDL with (a) early and (b) late endosomes, and (c) lysosomes using a confocal super-resolution microscope. Endosomes and lysosomes were visualized by transduction with a viral vector encoding GFP-fused indicated proteins in CHO-LOX-1-AT1 (CellLight™, Thermo Fisher Scientific, USA). After 30 min of treatment with 2 μg/ml Dil-labeled oxLDL, cells were washed and fixed immediately (early phase, 0 min) or after 5 h of additional incubation without oxLDL (late phase, 5 h). Approximate cell boundaries are marked with dotted lines. Yellow (merged) puncta in overlaid images indicate co-localization of oxLDL with each organelle.

(left lower panels) Representative images, scale bar, μm. (right panels) Quantification of proportion of merged puncta relative to total green (early, late endosomes or lysosomes) or red puncta (oxLDL) (n = 9–10, each group), analyzed as described in the methods. 0 m, early phase (0 min); 5 h, late phase (5 h);.Data are represented as mean +/- SEM. The differences were determined by Student's t-test. $^{*}p < 0.05$ vs. the others

Figure S2: Cellular accumulation of Dil-oxLDL was blocked by non fluorescent oxLDL in CHO. Related to Figure 5.

Intracellular uptake of Dil-labeled oxLDL in CHO-LOX-1-AT1 with or without simultaneous treatment with non-fluorescent oxLDL (n = 4, each). Scale bar, μm

The graph indicates the fluorescence/number of nuclei, and the average value of the group at the far left was normalized to 100%. Data are represented as mean +/- SEM. The differences were determined by one-way ANOVA with Bonferroni correction. $^*p < 0.01$ vs. treatment without non-fluorescent oxLDL

NF-oxLDL, non-fluorescent oxLDL
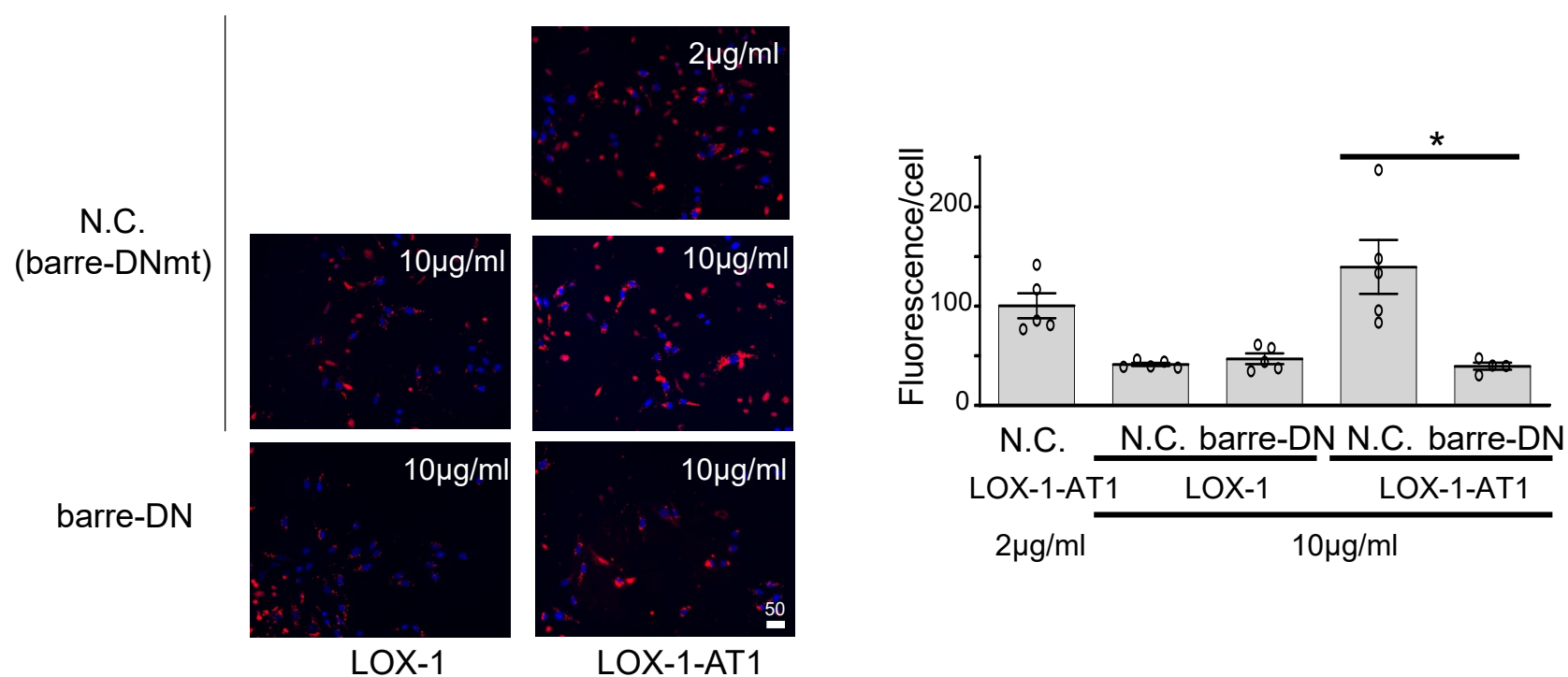
Figure S3: AT1-independent uptake of a higher concentration of oxLDL via LOX-1 was β-arrestin independent in CHO. Related to Figure 5.

Intracellular uptake of Dil-labeled oxLDL at the indicated concentrations in CHO-LOX-1 or CHO-LOX-1-AT1 transfected with dominant negative vector of β-arrestin (barre-DN) or negative control vector (N.C.) (n = 5, each). Scale bar, μm

The graph indicates the fluorescence/number of nuclei, and the average value of the group at the far left was normalized to 100%. Data are represented as mean +/- SEM. The differences were determined by one-way ANOVA with Bonferroni correction. *$p < 0.01$
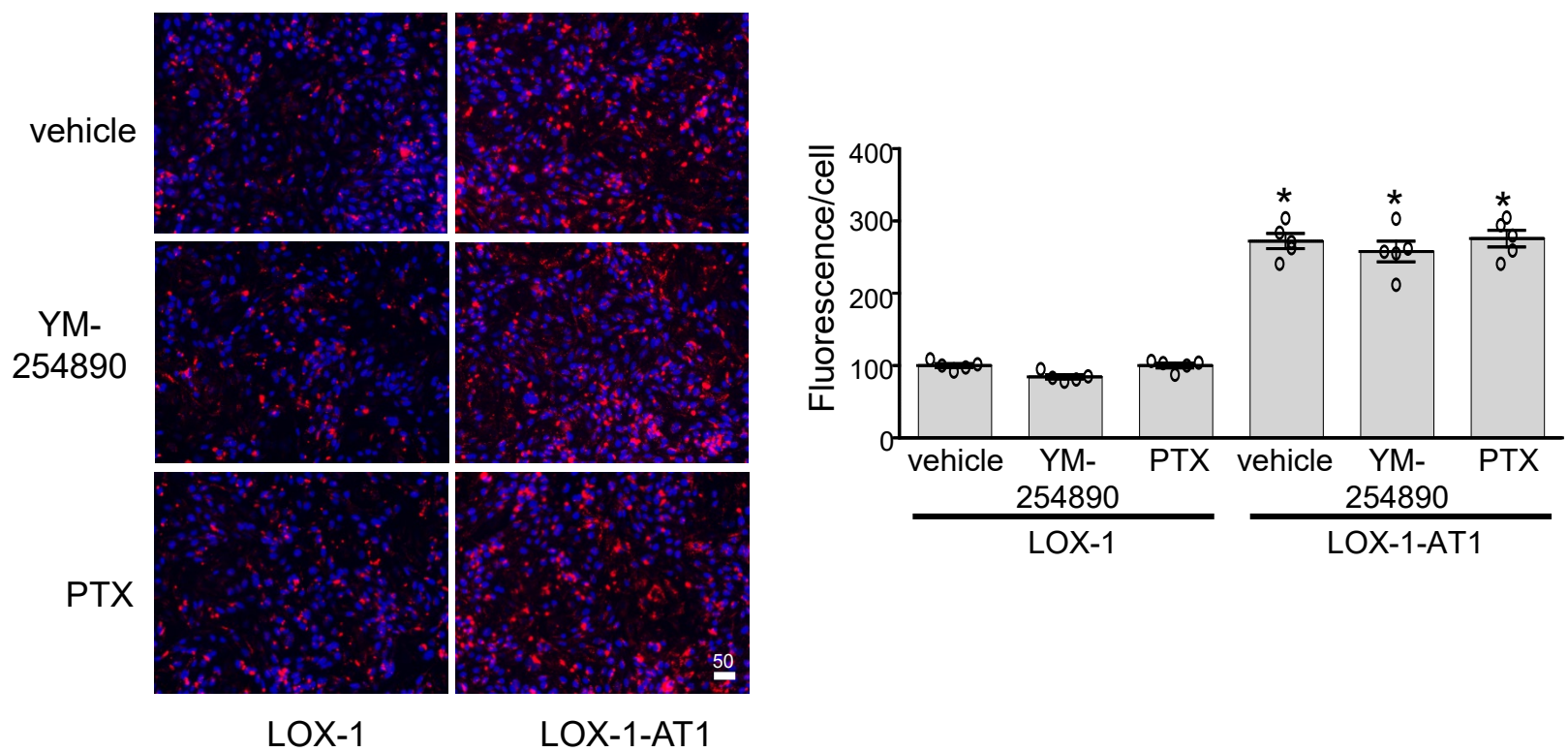
Figure S4: Cellular accumulation of oxLDL was independent of Gαi and Gαq-dependent pathways in CHO.

Related to Figure 5.

Intracellular uptake of Dil-labeled oxLDL at the indicated concentrations in CHO-LOX-1 or CHO-LOX-1-AT1

pretreated with vehicle, Gq inhibitor, YM254890, or Gi inhibitor, pertussis toxin (PTX) (n = 5, each). Scale bar, μm

YM-254890 and PTX were pretreated at 1 μM and 25 ng/ml for 30 min and 12 h before stimulation, respectively.

The graph indicates the fluorescence/number of nuclei, and the average value of the group at the far left was

normalized to 100%. Data are represented as mean +/- SEM. The differences were determined by one-way ANOVA

with Bonferroni correction. $^*p < 0.01$ vs. treatment-matched wells in CHO-LOX-1
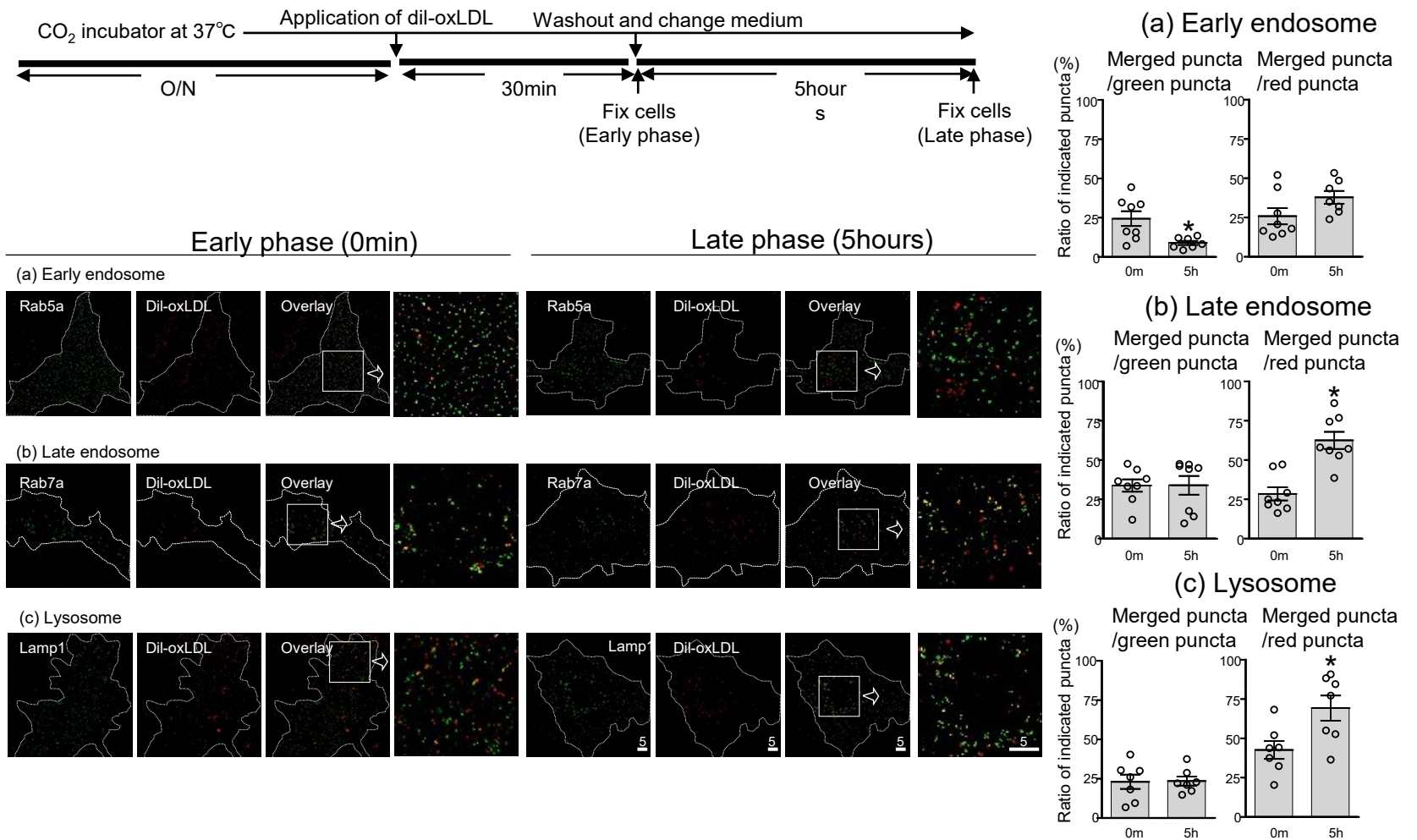
Figure S5: Endocytic traffic of oxLDL with early endosomes, late endosomes and lysosome in HUVECs. Related to Figure 6.

Visualization of co-localization of oxLDL with (a) early and (b) late endosomes, and (c) lysosomes using a confocal super-resolution microscope. Endosomes and lysosomes were visualized after transduction of a viral vector encoding GFP-fused indicated proteins in human umbilical vein endothelial cells (HUVECs) (CellLight™, Thermo Fisher Scientific, USA). After 30 min of treatment with 2 μg/ml Dil-labeled oxLDL, cells were washed and fixed immediately (early phase, 0 min) or after 5 h of additional incubation without oxLDL (late phase, 5 h). Approximate cell boundaries are marked with dotted lines. Yellow (merged) puncta in overlaid images indicate co-localization of oxLDL with each organelle.

(left lower panels) Representative images, scale bar, μm. (right panels) Quantification of proportion of merged puncta relative to total green (early, late endosomes or lysosomes) or red puncta (oxLDL) (n = 9–10, each group), analyzed as described in the methods. 0 m, early phase (0 min); 5 h, late phase (5 h);.Data are represented as mean +/- SEM. The differences were determined by Student's t-test. $^{*}p < 0.05$ vs. the others

Figure S6: The siRNA-mediated knockdown efficiency of indicated genes in HUVECs and HAECs. Related to Figure 6.

(a–d) Confirmation of the efficiency of siRNA-mediated knockdown of indicated genes by quantitative real-time PCR in human umbilical vein endothelial cells (HUVECs) and human aortic endothelial cells (HAECs) (n = 4–5, each). (a) siRNA against *AT1* decreased *ARRB1* expression in HUVECs and HAECs, and increased *ARRB2* expression in HUVECs, suggesting an undetermined interaction at the transcriptional level. (c) siRNA against *GRK2* or *GRK3* decreased GRK3 or GRK2 levels in HUVECs and HAECs, respectively, suggesting an interaction at the transcriptional level. The expression level of each gene was normalized using *GAPDH* mRNA as an internal control. Data are represented as mean +/- SEM. Differences with respect to the relative gene expression of cells treated with scramble siRNA (si-scramble) were determined by one-way ANOVA with Bonferroni correction. *$p < 0.01$, †$p < 0.05$
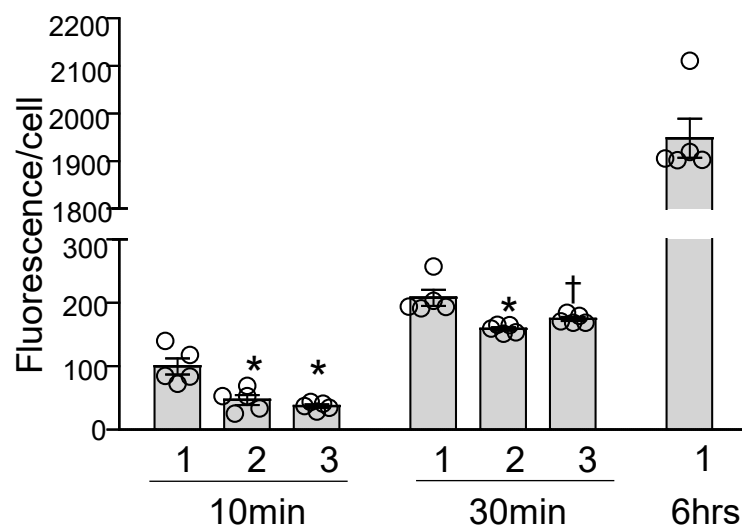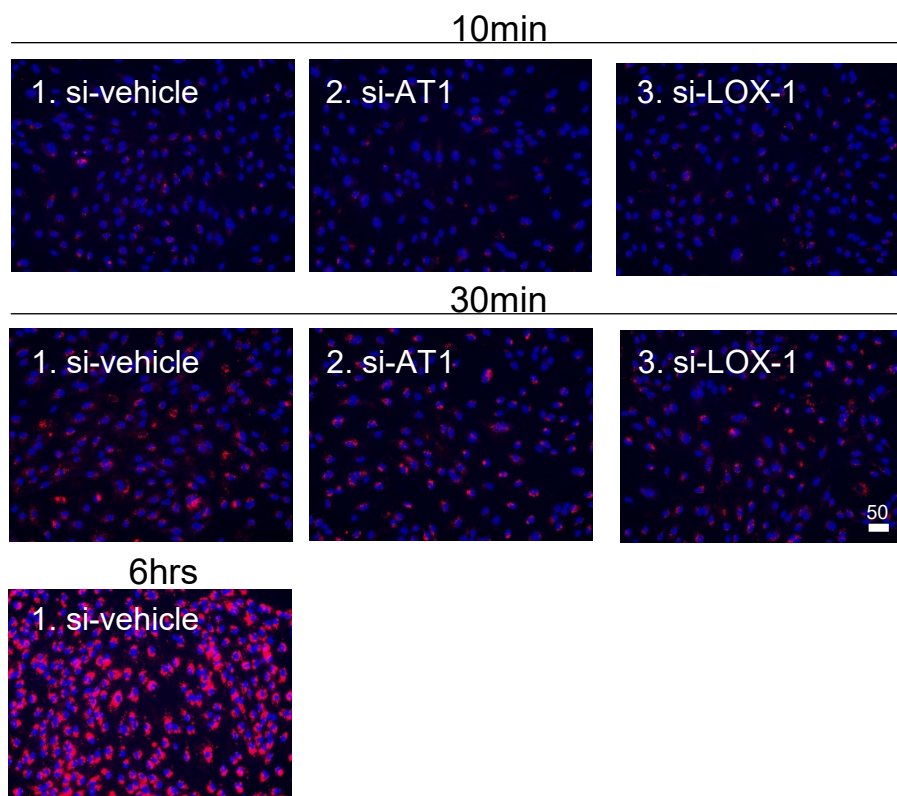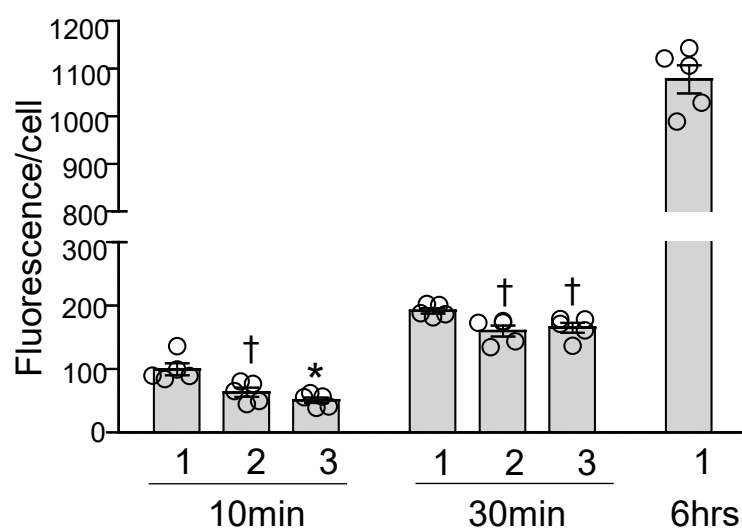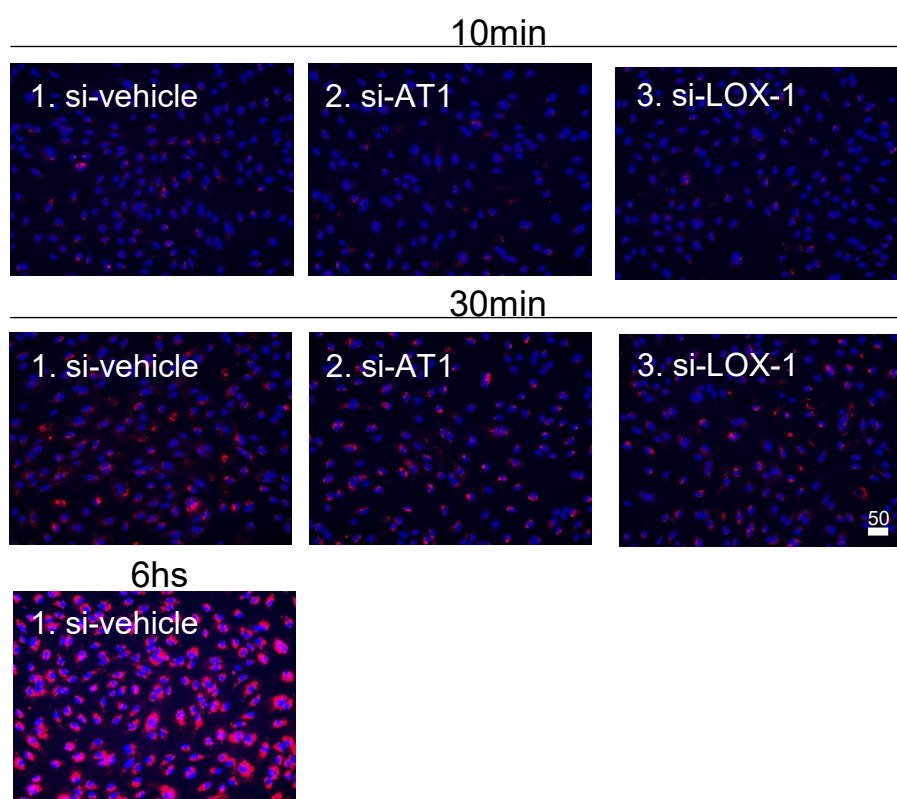
Figure S7: The inhibitory effect of siRNA against AT1 or LOX-1 in HUVECs and HAECs. Related to Figure 6.

Intracellular uptake of 2 µg/ml Dil-labeled oxLDL treated for three different durations to human umbilical vein endothelial cells (HUVECs) and human aortic endothelial cells (HAECs) with siRNA-mediated knockdown of the indicated genes (n = 5, each). Scale bar, µm

The graph indicates the fluorescence/number of nuclei, and the average value of the group at the far left was normalized to 100%. Data are represented as mean +/- SEM. The differences were determined by one-way ANOVA with Bonferroni correction $^*p < 0.01$ vs. control in each time course, $\dagger p < 0.05$ vs. control in each time course
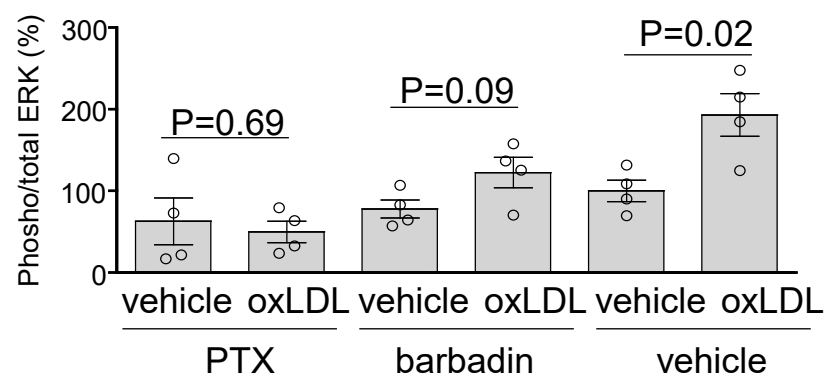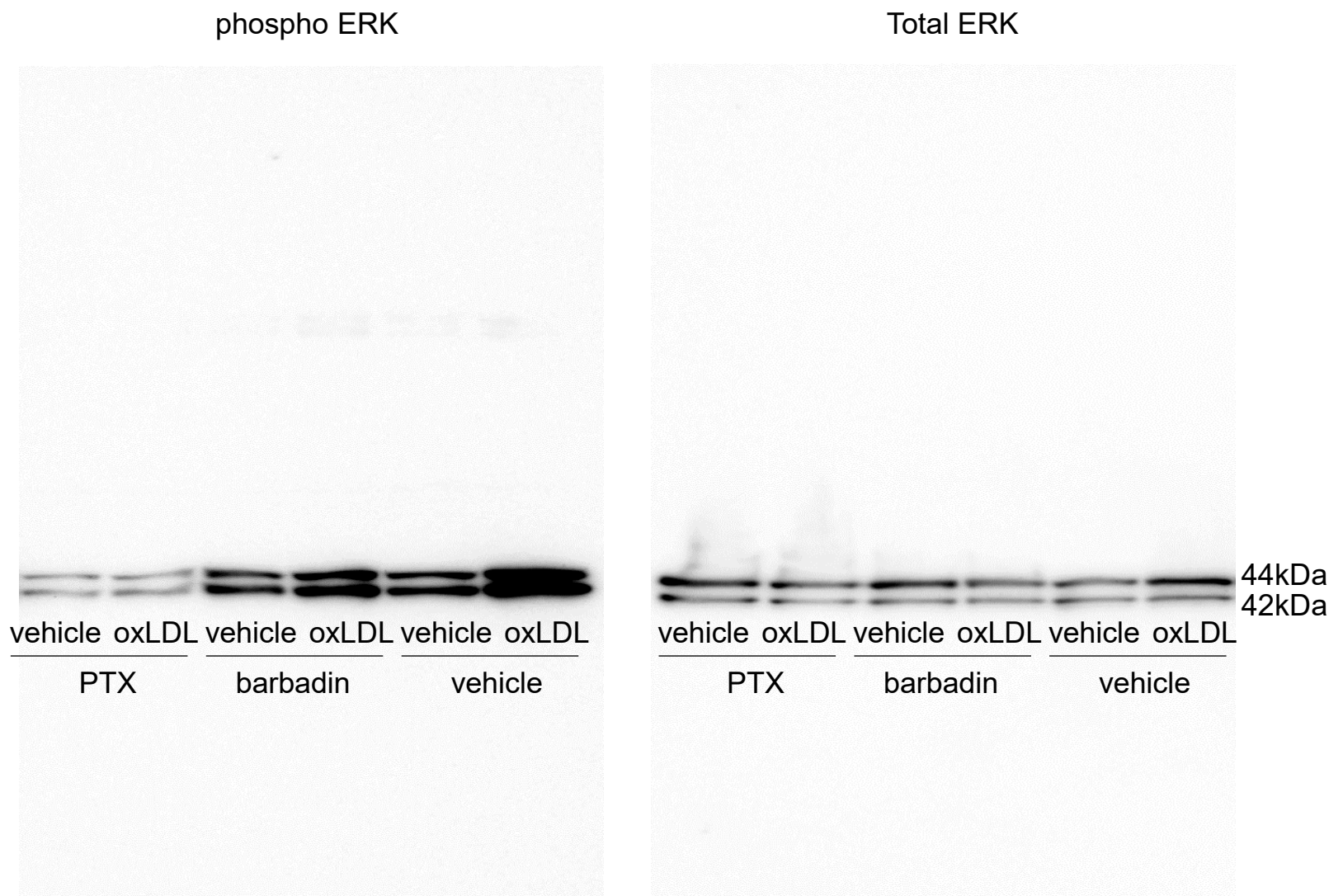
Figure S8: ERK1/2 activation induced by oxLDL was inhibited either by a Gi-specific inhibitor or a β-arrestin inhibitor in HUVECs. Related to Figure 6.

Immunoblotting for detecting phosphorylation of extracellular signal-regulated kinase 1/2 in human umbilical vein endothelial cells (HUVECs). Cells were stimulated with vehicle or 20μg/ml oxLDL for 10 min after a 6-h pre-treatment with vehicle, 25 ng/ml PTX, a Gi inhibitor, or 10 μM barbadin, a β-arrestin inhibitor. (Upper panel) Representative immunoblots of phosphorylated ERK1/2 and total ERK1/2. (Lower panel) Quantification of ERK 1/2 activation by densitometric analysis of phosphorylated/total ERK 1/2. The average activation after vehicle treatment following vehicle pretreatment was set at 100%. Data are represented as mean +/- SEM. The difference in ERK1/2 activation between oxLDL-treated and vehicle-treated cells was determined by Student's t-test.

We confirmed that the antibodies for phosphorylated and total ERK1/2 visualize only the indicated two bands equivalent to the molecular weights of 42 and 44kDa.
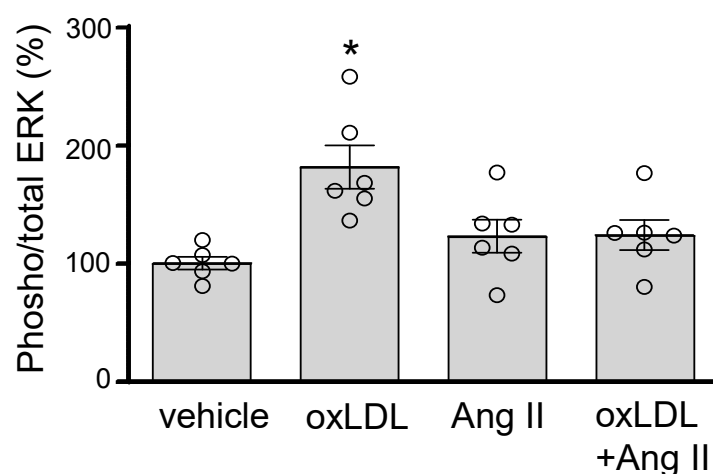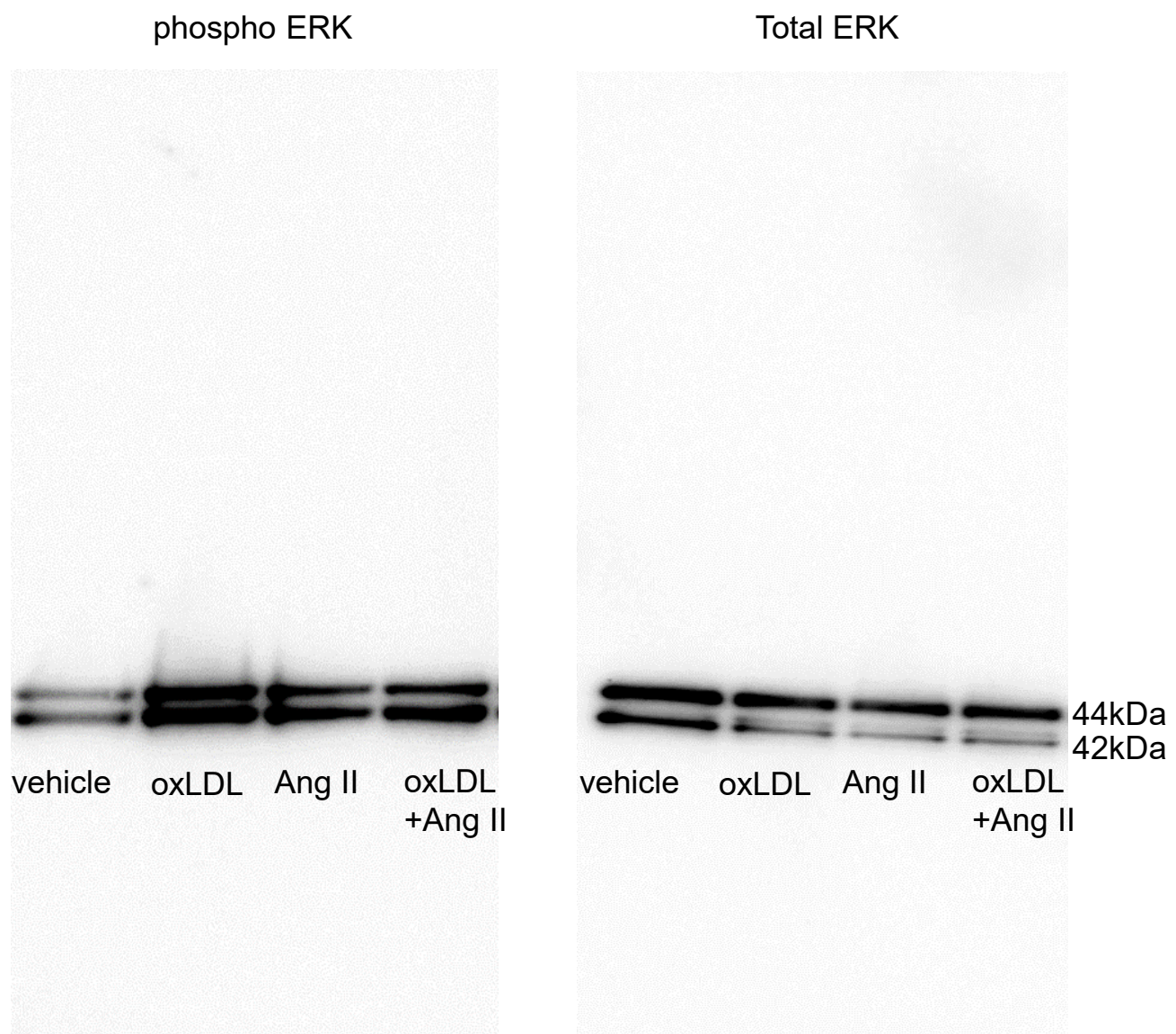
Figure S9: The effect of Ang II and oxLDL on cellular signaling was not additive but rather competitive in HUVECs. Related to Figure 6.

Immunoblotting for detecting phosphorylation of extracellular signal-regulated kinase 1/2 in human umbilical vein endothelial cells (HUVECs). Cells were stimulated with vehicle, 20μg/ml oxLDL, 10^{-7}M Ang II or oxLDL in combination with Ang II for 10 min. (Upper panel) Representative immunoblots of phosphorylated ERK1/2 and total ERK1/2. (Lower panel) Quantification of ERK 1/2 activation by densitometric analysis of phosphorylated/total ERK 1/2. The average activation after vehicle treatment following vehicle pretreatment was set at 100%. Data are represented as mean +/- SEM. Differences were determined by one-way ANOVA with Bonferroni correction. *$p < 0.01$ vs. control

We confirmed that the antibodies for phosphorylated and total ERK1/2 visualize only the indicated two bands equivalent to the molecular weights of 42 and 44kDa.
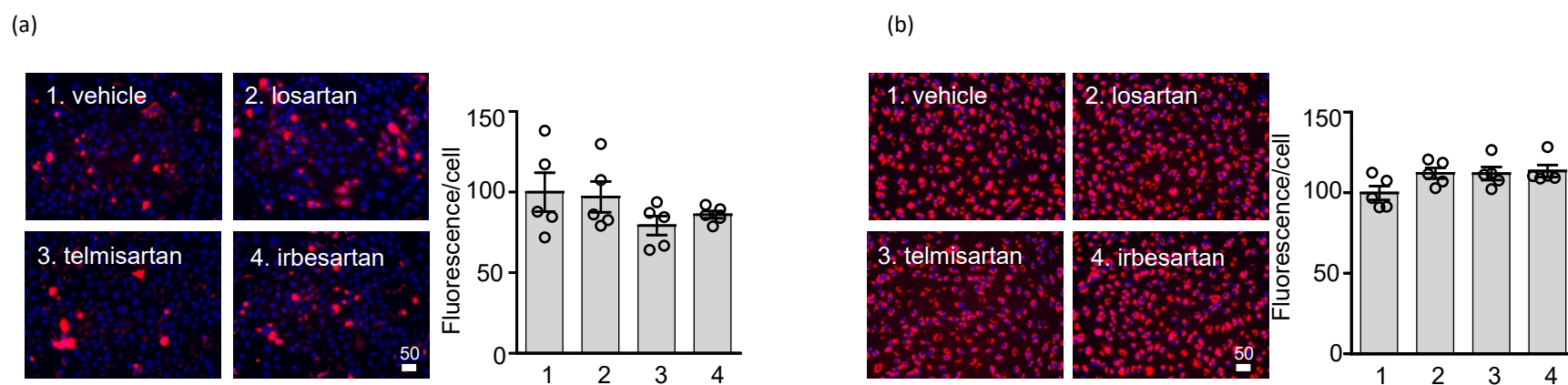
Figure S10: ARBs had no effect on oxLDL uptake in CHO or HUVECs. Related to Figure 6.

Intracellular uptake of 2 µg/ml Dil-labeled oxLDL in (a) CHO-LOX-1-AT1 or (b) HUVECs pretreated with vehicle or

10 µM AT1 blockers (ARBs) (n = 5, each). The graph indicates the fluorescence/number of nuclei, and the average

value of the group at the far left was normalized to 100%. Data are represented as mean +/- SEM. The differences were
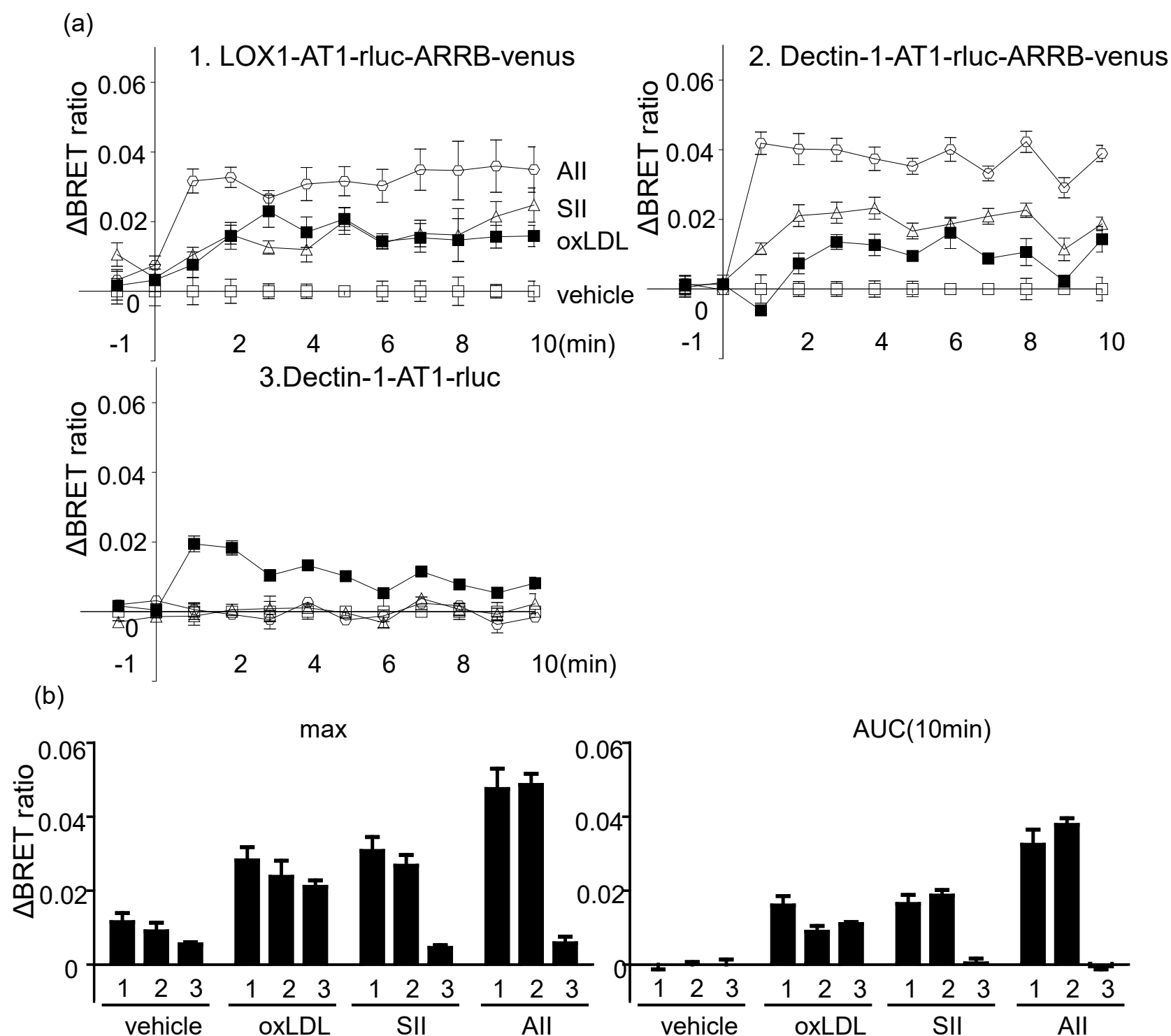
determined by one-way ANOVA.

Figure S11:oxLDL-induced BRET between AT1-Rluc8 and β-arrestin 2 (ARRB2)-mVenus in CHO-K1 cells in the presence of LOX-1. Related to Figure 4.

(a) Kinetic data for real-time BRET assay. Coelenterazine h was added before measurement, and each reagent (vehicle, angiotensin II (Ang II) (10-5 M), SII, an arrestin-biased agonist of AT1 (10-5 M), or oxLDL (100 μg/ml)) was added immediately after 0 min. The ΔBRET ratio adjusted by that in vehicle treatment was calculated as described in the Online Methods (n = 8 in 1. LOX1-AT1-rluc-ARRB2-venus, and 2. Dectin-1-AT1-rluc-ARRB2-venus, n = 4 in 3. Dectin-1-AT1-rluc (without ARRB2-venus)).

(b) Comparison of ΔBRET ratios among cells transfected with 1. LOX1-AT1-rluc-ARRB2-venus, 2. Dectin-1-AT1-rluc-ARRB2-venus, and 3. Dectin-1-AT1-rluc. Max BRET ratio and area under the curve (AUC) at 1–10 min are presented. There were no significant differences in max and AUC of the ΔBRET ratio among the transfection in response to oxLDL. Data are represented as mean +/- SEM. The differences were determined by one-way ANOVA.